JGR | Machine Learning and Computation

RESEARCH ARTICLE
10.1029/2024JH000275

Seismic Reservoir Characterization With Implicit Neural Representations

Juan Romero[1], **Wolfgang Heidrich**[1], **Nick Luiken**[1,2], **and Matteo Ravasi**[1]

[1]King Abdullah University of Science and Technology (KAUST), Thuwal, Saudi Arabia, [2]NVIDIA, Dubai, UAE

Abstract Seismic reservoir characterization refers to a set of techniques aimed at estimating static and/or dynamic physical properties of subsurface geological formations from seismic data, with applications ranging from exploration and development of energy resources, geothermal production, carbon capture and storage, and the assessment of geological hazards. Extracting quantitative information from seismic recordings, such as an acoustic impedance model, is however a highly ill-posed inverse problem due to the band-limited and noisy nature of the seismic data. As such, seismic inversion techniques strongly rely on additional prior information that penalizes (or promotes) some features in the recovered model. This paper introduces IntraSeismic, a novel hybrid seismic inversion method that combines implicit neural representations as an effective way to parameterize a subsurface model with the physics of the seismic modeling operator. We demonstrate its effectiveness in both pre-stack and 3D/4D post-stack seismic inversion using synthetic and field data sets. Key features of IntraSeismic are (a) unparalleled performance in 2D and 3D pre-stack/post-stack dynamic and static seismic inversion, (b) rapid convergence rates, (c) ability to seamlessly include hard constraints (i.e., well data) and perform uncertainty quantification, and (d) potential data compression and fast randomized access to specific portions of the inverted model.

Plain Language Summary Geoscientists use sound waves to detect underground structures with the objective of finding energy resources or storing carbon dioxide. However, extracting quantitative information from this data can be challenging. Our research introduces IntraSeismic, a new method that uses novel techniques in artificial intelligence to create a more accurate picture of such underground formations. IntraSeismic is faster and more accurate than existing methods at extracting rock properties from sound wave data. This allows scientists to make better decisions about resources hidden beneath the Earth's surface.

Key Points:

- Introduce a novel, compact representation for subsurface properties by means of implicit neural networks (Implicit neural representation (INR))
- Regularize ill-posed seismic inverse problems by leveraging INR, whilst ensuring physical consistency with the seismic modeling operator
- Highlight the additional benefits of using INR in seismic inversion, like data compression and improved uncertainty estimation, among others

This study was conducted by Nick Luiken while he was affiliated with KAUST.

Supporting Information:

Supporting Information may be found in the online version of this article.

Correspondence to:

J. Romero,
juan.romeromurcia@kaust.edu.sa

Citation:

Romero, J., Heidrich, W., Luiken, N., & Ravasi, M. (2024). Seismic reservoir characterization with implicit neural representations. *Journal of Geophysical Research: Machine Learning and Computation*, *1*, e2024JH000275. https://doi.org/10.1029/2024JH000275

Received 14 MAY 2024
Accepted 26 JUL 2024

1. Introduction

A variety of seismic imaging techniques have been developed over the years and found applications in several industrial sectors to aid oil and gas prospecting (Sheriff & Geldart, 1995; Telford et al., 1990; Yilmaz, 2001) geotechnical assessment in civil engineering (Oz & Miller, 2015), construction projects (Steeples & Miller, 1988), and more recently, geothermal production and carbon capture and storage monitoring (Lumley, 2010). Seismic inversion represents the foremost method for deriving quantitative information from seismic data (Tarantola, 1984). A seismic inverse problem endeavors to approximate the elastic parameters of the subsurface, such as wave propagation velocities and density, from either raw or processed seismic data (Doyen, 2007). These elastic parameters are crucial for comprehensive reservoir characterization, where petrophysical properties such as porosity and saturation can be further estimated (Grana et al., 2021, 2022). This usually requires a rock physics model, which establishes a theoretical link between elastic and petrophysical parameters (Avseth et al., 2005; Bosch et al., 2010). Thus, seismic inversion combined with rock physics models provides a powerful tool for enhancing our understanding of subsurface properties and improving the accuracy of reservoir predictions.

When seismic inversion is carried out post-migration (i.e., after the raw data set has been imaged), the associated inverse problem, called *pre-stack or post-stack seismic inversion*, is highly ill-posed due to the limited range of frequencies excited in a seismic experiment and the inevitable presence of noise in the data. Historically, this problem has been tackled through three distinct families of methods: (a) variational methods, (b) deep learning-based approaches, and (c) hybrid methods. Variational methods aim to minimize a data-misfit term accompanied by one or more regularization terms that guide the solution to a physically plausible outcome. A standard regularization choice is Tikhonov regularization (Tikhonov & Arsenin, 1977), which favors the retrieval of a smooth

subsurface model. More recently, total variation (TV) regularization (Rudin et al., 1992) has been used to enforce a layered structure of the subsurface, which is a more realistic representation of the acoustic impedance (Gholami, 2015; Ravasi & Birnie, 2022; Wang et al., 2019). Deep learning-based approaches, on the other hand, leverage the prowess of neural networks to learn a direct mapping between the seismic data and acoustic impedance model, providing that a suitable training data set is available. Various architectures have been used so far in the literature, including XGBoost (Zhao et al., 2021), convolutional neural networks (Biswas et al., 2019; Das et al., 2019; Xu et al., 2022), temporal convolutional networks (R. Smith et al., 2022), and attention-based networks (Wu et al., 2022). However, seismic applications deal with a shortage of labeled data sets because the ground truth is inaccessible except for specific locations along drilled wells. Consequently, the application of supervised learning approaches is limited in this domain and is feasible only when a dense well coverage is available (Ravasi, Luiken, et al., 2023). Hybrid seismic inversion methodologies harness the strengths of both paradigms by amalgamating the foundational geological knowledge and physics-based modeling with the pattern recognition capabilities of deep learning techniques. An example of hybrid methods is the Deep Image Prior (DIP) (Ulyanov et al., 2020), which uses a neural network as a nonlinear preconditioner in the solution of an inverse problem and has been successfully applied to the post-stack seismic inversion problem (Lipari et al., 2021). Similarly, the Plug-and-Play (PnP) framework (Venkatakrishnan et al., 2013) has recently been proposed to solve inverse problems using a denoiser to act as a regularizer; this concept has led to the seamless inclusion of pre-trained deep denoisers (Zhang et al., 2022) in the solution of inverse problems of any kind: Romero, Corrales, et al. (2022) showed that this is also beneficial to 2D post-stack seismic inversion, achieving state-of-the-art results. For an extensive comparison of some of the previously described methods, we refer the reader to (Ravasi, Luiken, et al., 2023; Ravasi, Romero, et al., 2023).

These hybrid methods represent a forward-thinking direction for seismic inversion applications. Model-driven components ensure inversion results to be grounded in well-understood geophysical principles, providing interpretable and physically plausible solutions. Simultaneously, deep-learning-based components can capture complex, nonlinear relationships in the data and/or model that might be overlooked or overly simplified in purely model-driven techniques. In this spirit, we introduce IntraSeismic, a hybrid method that is able to:

- Leverage the power of INRs to solve ill-posed seismic inverse problems whilst retaining the physics of the seismic modeling operator through a modular framework.
- Seamless integrate hard constraints in the seismic inversion process.
- Perform Uncertainty quantification (UQ) via Monte Carlo Dropout (MCD).
- Provide a compact representation of subsurface models, serving as an efficient data compression mechanism.

This paper starts with an overview of pre-stack and post-stack seismic inversion, 4D seismic inversion, INRs, and their application to inverse problems. Following this introduction, we first provide a suite of numerical examples to demonstrate that IntraSeismic can outperform standard variational methods and other hybrid approaches in the inversion of post-stack seismic data with varying noise levels, both in terms of reconstruction quality and convergence rate. Then, we validate the effectiveness of our proposed method for pre-stack seismic inversion and 4D post-stack seismic inversion for synthetic and field data. We conclude by highlighting IntraSeismic's capabilities in incorporating hard constraints, performing UQ, serving as an efficient data compressor, and commenting on promising future research directions.

2. Theoretical Background

2.1. Pre-Stack Seismic Inversion

Post-migration angle-dependent seismic data $d_\theta(t)$ can be mathematically represented via the so-called convolutional model (Goupillaud, 1961). This entails the convolution of a source function or wavelet $w(t)$ with the earth P-wave reflectivity series $r_{pp}(t)$:

$$d_\theta(t) = w(t) * r_{pp}(t) \tag{1}$$

The Aki-Richards approximation (Aki & Richards, 2002), which builds on the foundational Zoeppritz equation (Zoeppritz, 1919), expresses r_{pp} as follows:

$$r_{pp}(t,\theta) = \sum_{i=1}^{3} c_i(t,\theta)\frac{d}{dt}\log(m_i(t)), \tag{2}$$

where the mixing coefficients c_i are given by

$$\begin{aligned} c_1(t,\theta) &= \frac{1}{2}\left(1 + \tan^2(\theta)\right) \\ c_2(t,\theta) &= -4\left(\frac{\bar{V}_s(t)}{\bar{V}_p(t)}\right)^2 \sin^2(\theta) \\ c_3(t,\theta) &= \frac{1}{2} - 2\left(\frac{\bar{V}_s(t)}{\bar{V}_p(t)}\right)^2 \sin^2(\theta) \end{aligned} \tag{3}$$

and

$$\mathbf{m}(t) = (V_p(t), V_s(t), \rho(t)), \tag{4}$$

where θ represents the incidence angle of the seismic raypath, $V_p(t)$ is the P-wave velocity, $V_s(t)$ the S-wave velocity, and $\rho(t)$ is the density of the medium of interest. For convenience, let us define the dimensions: N_θ represents the number of incidence angles considered, and N_y, N_x, and N_t are the spatial dimensions. A reduced matrix-vector form of the pre-stack data equation, previously introduced as Equation 1, is represented as:

$$\mathbf{d}_\theta = \mathbf{W}_\theta \mathbf{C}\mathbf{D}\mathbf{m}, \tag{5}$$

where $\mathbf{d}_\theta \in \mathbb{R}^{N_\theta N_y N_x N_t}$ is the data vector for different angles and $\mathbf{m} = [\mathbf{V_p}, \mathbf{V_s}, \boldsymbol{\rho}]^T \in \mathbb{R}^{3N_y N_x N_t}$ is the model parameter vector. The operator $\mathbf{W}_\theta \in \mathbb{R}^{N_\theta N_y N_x N_t \times N_\theta N_y N_x N_t}$ is a block diagonal matrix with convolution operators for every angle θ. The mixing operator $\mathbf{C} \in \mathbb{R}^{N_\theta N_y N_x N_t \times 3N_y N_x N_t}$ contains the coefficients that linearly combine the effects of $\mathbf{V_p}$, $\mathbf{V_s}$ and $\boldsymbol{\rho}$ on the seismic response, as detailed in Equation 3. The operator $\mathbf{D} \in \mathbb{R}^{3N_y N_x N_t \times 3N_y N_x N_t}$ is a block diagonal matrix comprising the first derivative matrices. The pre-stack seismic inverse problem is therefore represented as:

$$\mathbf{m}^* = \underset{\mathbf{m}}{\operatorname{argmin}} \frac{1}{2}\|\mathbf{W}_\theta C D m - \mathbf{d}_\theta\|_2^2 + \alpha \mathcal{R}(\mathbf{m}), \tag{6}$$

where $\mathcal{R}(\mathbf{m})$ is the regularization term and α is the regularization parameter, controlling the level of regularization applied.

2.2. Post-Stack Seismic Inversion

When only zero offset data is considered, that is, $\theta = 0$, Equation 2 becomes:

$$r_{PP} = \frac{1}{2}\frac{d}{dt}\log(m(t)), \tag{7}$$

where r_{PP} is referred in this case as post-stack reflectivity and $m(t)$ is the P-wave or acoustic impedance. Post-stack seismic data is hence modeled as:

$$d(t) = \frac{1}{2}w(t) * \frac{d}{dt}\log(m(t)) \tag{8}$$

In compact matrix-vector notation:

$$\mathbf{d} = \mathbf{W}\mathbf{D}\mathbf{m}, \tag{9}$$

where $\mathbf{W} \in \mathbb{R}^{N_y N_x N_t \times N_y N_x N_t}$ is a single block-Toeplitz convolution matrix, which encapsulates the seismic wavelet, while $\mathbf{D} \in \mathbb{R}^{N_y N_x N_t \times N_y N_x N_t}$ is a single first-order derivative operator. Post-stack seismic inversion transforms seismic images $\mathbf{d} \in \mathbb{R}^{N_y N_x N_t}$ into quantitative estimates of the subsurface's acoustic impedance $\mathbf{m} \in \mathbb{R}^{N_y N_x N_t}$ (Oldebnbur et al., 1983; Russell & Hampson, 1991), and it is expressed as:

$$\mathbf{m}^* = \underset{\mathbf{m}}{\operatorname{argmin}} \frac{1}{2} \|\mathbf{WDm} - \mathbf{d}\|_2^2 + \alpha \mathcal{R}(\mathbf{m}), \tag{10}$$

The objective of Equations 6 and 10 is to minimize the discrepancy between the modeled and observed seismic data, adjusted by a regularization term $\mathcal{R}(\mathbf{m})$. Typically, the pre-stack ($\mathbf{W_0CD}$) and post-stack ($\mathbf{WD}$) seismic modeling operators are collectively represented by an operator $\mathbf{G}$, to simplify their notation.

2.3. Simultaneous 4D Seismic Inversion

In the context of 4D post-stack seismic inversion, there exist at least two data sets, $\mathbf{d_1}$ and $\mathbf{d_2}$, which have been acquired at different times over the same geographical area. The associated inverse problem involves estimating the underlying acoustic impedance models, $\mathbf{m_1}$ and $\mathbf{m_2}$, through an augmented form of Equation 10:

$$\underset{\mathbf{m_1},\mathbf{m_2}}{\operatorname{argmin}} \frac{1}{2} \left\| \begin{bmatrix} \mathbf{G_1} & \mathbf{0} \\ \mathbf{0} & \mathbf{G_2} \end{bmatrix} \begin{bmatrix} \mathbf{m_1} \\ \mathbf{m_2} \end{bmatrix} - \begin{bmatrix} \mathbf{d_1} \\ \mathbf{d_2} \end{bmatrix} \right\|_2^2 + \alpha \mathcal{R}(\mathbf{m_1}, \mathbf{m_2}), \tag{11}$$

where $\mathbf{G_1}$ and $\mathbf{G_2}$ are the post-stack seismic modeling operators for both data sets respectively. Note that the two operators might have different wavelets $w_1(t)$ and $w_2(t)$. $\mathcal{R}(\mathbf{m_1}, \mathbf{m_2})$ is the regularization that assures the coupling between both models $\mathbf{m_1}$ and $\mathbf{m_2}$, and α is the regularization parameter or weight.

2.4. Implicit Neural Representations for Inverse Problems

Implicit neural representations or coordinate-based learning, wherein neural networks directly utilize spatial coordinates as input, has emerged as a focal point in recent deep learning advancements (Sitzmann et al., 2020; Tancik et al., 2020; Xie et al., 2021). This approach has achieved state-of-the-art results in various domains, including image and shape representation (Chen & Zhang, 2019; Park et al., 2019) and volume density, and view synthesis (Mildenhall et al., 2020), to name a few. Neural Radiance Fields (Mildenhall et al., 2020) is an example of pioneering work in this domain, which has showcased the potent application of spatial coordinates in rendering photo-realistic 3D scenes. The main idea behind INRs is to learn a mapping $f_\theta(\boldsymbol{x}) : \mathbb{R}^d \rightarrow \mathbb{R}^m$ where f_θ consists of an encoding process—either trainable or non-trainable—followed by a multi-layer perceptron (MLP) to generate the output value (e.g., color intensity in an image). The input coordinate $\boldsymbol{x}$ may vary in dimensionality: it can be a 2D array for images, 3D for volumes and videos, and 5D in the case of Neural Radiance Fields.

A recent notable contribution to the inverse problems field is the IntraTomo framework (Zang et al., 2021). IntraTomo synergizes a coordinate-based MLP to estimate a density field with a subsequent geometry refinement module that solves an optimization problem to refine the details in such a density field. The data- and model-driven combination of IntraTomo has achieved state-of-the-art results in computer tomography. In the domain of seismic inversion, a parallel methodology has been suggested, involving the inversion of full-waveform seismic data using spatial coordinates as inputs to an MLP with variable activation functions (J. Sun et al., 2023).

In the present study, we draw inspiration from IntraTomo and further develop this concept to produce a new technique called "IntraSeismic." In IntraSeimic, we take further advantage of the recently introduced multi-resolution hash encoding mechanism with trainable feature vectors as a way to enrich the expressiveness of the network's input (Müller et al., 2022). As such, we are able to employ a very small, streamlined MLP architecture with two layers of 64 neurons each. Finally, we assimilate the "geometry refinement module" of IntraTomo, by directly embedding model-based regularization terms in the neural network's loss function. Consequently, IntraSeismic emerges as a compact and computationally efficient framework that is tailor-made for solving highly ill-posed inverse problems in geophysics.

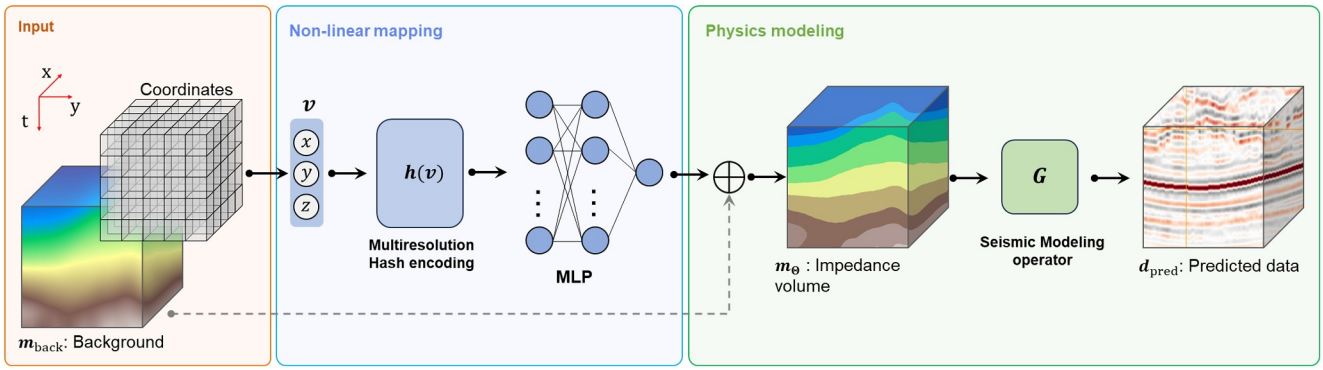

Figure 1. Schematic representation of the IntraSeismic framework: the input to IntraSeismic consists of spatial coordinates that are processed through a nonlinear mapping module. Initially, this module maps the input coordinates into a higher-dimensional space of trainable feature vectors using multiresolution hash encoding. Subsequently, these vectors are fed to a multi-layer perceptron (MLP) that outputs the impedance model. In the subsequent physics modeling module, the output from the MLP is added to the background model. A modeling operator then computes the predicted data from the impedance model, which is then incorporated into the loss function.

3. Methodology

The IntraSeismic framework (Figure 1) integrates INRs with a seismic modeling operator to invert seismic data for subsurface models of physical properties. The proposed framework primarily uses coordinates as input, which first undergo a multi-resolution hash encoding process (Müller et al., 2022). Next, the encoded coordinates are passed through an MLP, whose output is added to a user-provided background model and subsequently fed to the seismic modeling operator to allow evaluation of the loss function. The fundamental framework described here serves as the foundation for both single-parameter and multi-parameter seismic inversion, which will be elaborated in the following.

3.1. Single-Parameter Seismic Inversion

For the case of post-stack seismic inversion, the IntraSeismic loss function is formulated as:

$$\begin{aligned} &\underset{\Theta}{\operatorname{argmin}} \frac{1}{2}\|\mathbf{G}\boldsymbol{m}_\Theta - \mathbf{d}\|_2^2 + \alpha\mathcal{R}(\boldsymbol{m}_\Theta) \\ &\boldsymbol{m}_\Theta = \mathbf{F}_\Theta(\boldsymbol{x}) + \boldsymbol{m}_{\text{back}}, \end{aligned} \tag{12}$$

where $\boldsymbol{m}_\Theta$ denotes the subsurface acoustic impedance volume obtained from the inversion process, $\mathbf{F}_\Theta(\boldsymbol{x})$ is the non-linear mapping module with Θ representing the learnable parameters from both the hash table and the MLP, and $\mathbf{x} \in \mathbb{R}^{N_y N_x N_t \times 3}$ corresponds to the spatial coordinates of the volume of interest. These coordinates can be processed in IntraSeismic either as a single batch or in mini-batches. The term $\boldsymbol{m}_{\text{back}}$ refers to the background model. The regularization term, $\mathcal{R}(\boldsymbol{m}_\Theta)$, employs anisotropic TV regularization on the model $\left(\mathcal{R}(\boldsymbol{m}_\Theta) = \|\boldsymbol{m}_\Theta\|_{TV}\right)$ to achieve a high-resolution layered representation of the subsurface. Our experiments demonstrate improved performance when incorporating additional regularization on the MLP output, such as sparsity-promoting regularization $\mathcal{R}(\mathbf{F}_\Theta(\boldsymbol{x})) = \|\mathbf{F}_\Theta(\boldsymbol{x})\|_1$, or dynamically scheduled L_2 regularization $\mathcal{R}(\mathbf{F}_\Theta(\boldsymbol{x})) = \beta_k \|\mathbf{F}_\Theta(\boldsymbol{x})\|_2^2$, where the regularization weight β diminishes across iterations k (for further details refer to the supplementary material).

3.2. Multiparameter Seismic Inversion

The IntraSeismic framework can be naturally extended to invert seismic data for multiple acoustic parameters (e.g., in 4D seismic inversion) or elastic properties (e.g., in pre-stack seismic inversion). This adaptation can be achieved in two alternative ways: using a single shared non-linear mapping module or using independent non-linear mapping modules for each inverted property. We compare both IntraSeismic implementations for pre-stack seismic inversion in Section 4.2.

3.2.1. Shared Mapping Module

The first approach leverages a single IntraSeismic non-linear mapping module $\mathbf{F}_\Theta$, to produce two or more subsurface properties. In this case, the base framework of IntraSeismic is preserved as in Figure 1, and regularization is applied to each property individually. For instance, in the context of pre-stack seismic inversion (referenced in 2.1), the objective is to simultaneously invert pre-stack seismic data for three key properties: $\boldsymbol{m} = [\mathbf{V_p}, \mathbf{V_s}, \boldsymbol{\rho}]^T$. This is achieved using a single non-linear mapping module that produces three distinct outputs: $\mathbf{F_{1\Theta}}$, $\mathbf{F_{2\Theta}}$, and $\mathbf{F_{3\Theta}}$. Consequently, Equation 12 is modified to accommodate for this multi-output strategy as follows:

$$\underset{\boldsymbol{\Theta}}{\operatorname{argmin}} \frac{1}{2} \left\| \mathbf{G} \begin{bmatrix} \mathbf{V_{p\Theta}} \\ \mathbf{V_{s\Theta}} \\ \boldsymbol{\rho}_{\boldsymbol{\Theta}} \end{bmatrix} - \mathbf{d} \right\|_2^2 + \alpha \mathcal{R}\left(\mathbf{V_{p\Theta}}, \mathbf{V_{s\Theta}}, \boldsymbol{\rho}_{\boldsymbol{\Theta}}\right) \tag{13}$$

where $\mathbf{V_{p\Theta}} = \mathbf{F_{1\Theta}} + \mathbf{V}_{\mathbf{p}back}$, $\mathbf{V_{s\Theta}} = \mathbf{F_{2\Theta}} + \mathbf{V}_{\mathbf{s}\text{back}}$, $\boldsymbol{\rho}_{\boldsymbol{\Theta}} = \mathbf{F_{3\Theta}} + \boldsymbol{\rho}_{\text{back}}$, $\boldsymbol{\Theta}$ are the IntraSeismic learnable parameters, and $\mathbf{V}_{\mathbf{p}\text{back}}$, $\mathbf{V}_{\mathbf{p}\text{back}}$, $\boldsymbol{\rho}back$ are the given P-wave, S-wave velocity and density background models.

3.2.2. Independent Mapping Modules

The second approach utilizes separate non-linear mapping modules for each property to be inverted; these modules are however still optimized in parallel. For instance, for the simultaneous 4D post-stack seismic inversion case with 2 data sets (baseline and monitor data sets), IntraSeismic is augmented with 2 parallel non-linear mapping modules. The first module aims to update a user-provided baseline background impedance model, whereas the second module is dedicated to predicting the 4D, or time-lapse, difference between the baseline and monitor impedance volumes. We call this new framework 4D-IntraSeismic 2 and the loss function is given by:

$$\underset{\boldsymbol{\Theta},\boldsymbol{\Phi}}{\operatorname{argmin}} \frac{1}{2} \left\| \begin{bmatrix} \mathbf{G_1} & \mathbf{0} \\ \mathbf{0} & \mathbf{G_2} \end{bmatrix} \begin{bmatrix} \mathbf{m}_{\boldsymbol{\Theta}} \\ \mathbf{m}_{\boldsymbol{\Theta}} + \mathbf{F}_{\boldsymbol{\Phi}} \end{bmatrix} - \begin{bmatrix} \mathbf{d_1} \\ \mathbf{d_2} \end{bmatrix} \right\|_2^2 + \alpha \mathcal{R}(\mathbf{m}_{\boldsymbol{\Theta}}, \mathbf{F}_{\boldsymbol{\Phi}}) \tag{14}$$

where $\mathbf{m}_\Theta = \mathbf{F}_\Theta(\mathbf{x}) + \mathbf{m}_{\text{back}}$ and $\mathcal{R}(\mathbf{m}_{\boldsymbol{\Theta}}, \mathbf{F}_{\boldsymbol{\Phi}}) = \|\mathbf{m}_\Theta\|_{TV} + \|\mathbf{m}_\Theta + \mathbf{F}_{\boldsymbol{\Phi}}\|_{TV} + \|\mathbf{F}_\Theta\|_1 + \|\mathbf{F}_{\boldsymbol{\Phi}}\|_1$. In this case, $\mathbf{m}_\Theta$ is the baseline acoustic impedance model, $\mathbf{F}_{\boldsymbol{\Phi}}$ is the 4D acoustic impedance difference, and $\boldsymbol{\Theta}$ and $\boldsymbol{\Phi}$ are the learnable parameters. We refer to this specific configuration of IntraSeismic for handling 4D data as 4D-IntraSeismic. Figure 2 shows a schematic representation of 4D-IntraSeismic. The TV regularization terms in $\mathcal{R}$ promote piecewise continuous representations for the baseline and monitor acoustic impedance models, enhancing the resolution across layers. The term $\|\mathbf{F}_\Theta\|_1$ promotes large variations in the inverted model, thus encouraging the retrieval of high-contrast impedance values, while $\|\mathbf{F}_\Phi\|_1$ ensures sparsity in the time-lapse difference. Note that extending 4D-IntraSeismic to multiple monitor surveys is trivial.

3.3. IntraSeismic Components

Input coordinates: A seismic data set is a 3D volume of spatial size N_y, N_x, N_t that can be represented via voxel discretization. Each voxel p_i within the volume is uniquely defined by its spatial coordinates $\boldsymbol{x_i} = (y, x, t)$. As shown in Equation 12, the collection of all coordinates of the volume of interest represents the input of the IntraSeismic framework. Note the third dimension N_t is time samples, as seismic data is usually inverted in time; however, this could be equivalently depth if we want to invert a depth domain seismic volume.

Background Model: A background or initial prior model plays a pivotal role in seismic inverse problems. This model must contain the low-frequency components of the subsurface impedance model, which are not captured in the data. In variational methods, the purpose of the background model is to steer the inverse process toward geologically consistent solutions. In this work, when considering synthetic data, the background model is obtained from a smoothed version of the ground truth. In contrast, for field data, the background model is derived

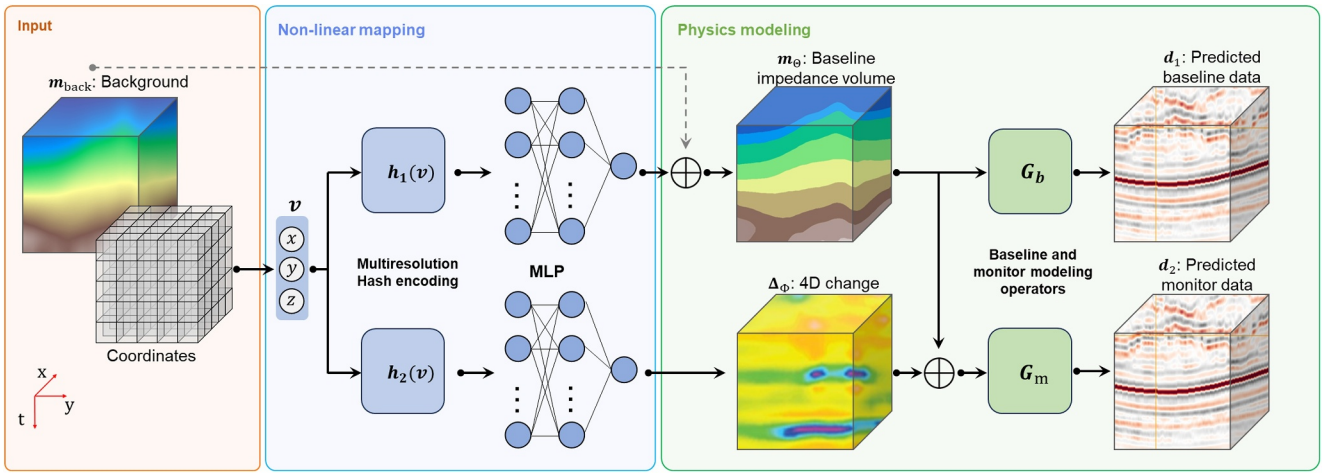

Figure 2. Schematic representation of the 4D-IntraSeismic framework: spatial coordinates are fed into a nonlinear mapping module, comprising two distinct sets of multiresolution hash encoding and multi-layer perceptron. The output from one set is summed to the background model to produce the baseline impedance model, whilst the output of the other set corresponds to the 4D impedance difference. These two outputs are then passed to the 4D seismic modeling module, which computes the predicted data.

from an interpolated, smoothed version of the impedance well-log data and/or a calibrated interval velocity volume from in-depth processing of the corresponding seismic data.

Multiresolution hash encoding: Encoding input coordinates into a higher-dimensional representation via predefined Fourier feature embeddings (or Gaussian-based alternatives) has been shown to significantly increase the ability of INRs to capture high-frequency information in the sought-after solution. Results are reported across a variety of computer vision tasks (Tancik et al., 2020; Mildenhall et al., 2020; Zheng et al., 2021; Y. Sun et al., 2021). Notably, Müller et al. (2022) introduced multiresolution hash encoding, a sparse grid-based parametric embedding that outperformed state-of-the-art non-parametric frequency-based encodings. This method utilizes a multi-resolution hash table with trainable feature vectors that are optimized through backpropagation, alongside the subsequent neural network parameters. This is accomplished by leveraging spatial hashing, where coordinates serve as the keys for a hash function, facilitating the retrieval of hash table indices. The hash function h for a coordinate point $\mathbf{x}$ is defined as:

$$h(\mathbf{x}) = \left(\bigoplus_{i=1}^{3} x_i \pi_i \right) \bmod T,$$

where $\oplus$ denotes the binary XOR operation, and π_i represents a large prime number chosen by the user. This function computes the indices for a hash table of size T that contains feature vectors of dimension F at every entry. Given its multi-resolution nature, this operation is performed at multiple predefined resolutions. Each input coordinate is scaled to a specific resolution, and through floor and ceiling operations, the surrounding points' corners at a given resolution are ascertained—yielding four corner points for a 2D problem and eight for a 3D problem. These corners are fed into the hash function, with the resultant feature vectors being interpolated to obtain the corresponding feature vector at the input point.

We leverage the multiresolution hash encoding hyperparameter settings suggested in Müller et al. (2022) for IntraSeismic. The encoding employs $L = 4$ levels of resolution, ranging from the coarsest ($N_{\min}$) to the finest ($N_{\max}$). The choice of $N_{\min}$ and $N_{\max}$ is guided by the size of the subsurface volume and the desired target resolution, such as the thickness of the finest geological layer to be retrieved. The hash table size (T) is set to 2^{16} entries, and each entry contains a feature vector of dimension $F = 2$.

Neural Network Architecture: The neural network component of IntraSeismic is a two-layer MLP with ReLU activation function. Each layer contains 64 neurons.

Table 1
Inversion Results for IntraSeismic and Benchmark Methods for the Marmousi and SEAM Data Sets and Different Noise Levels

	Marmousi			SEAM		
Method	$\sigma = 0$	$\sigma = 0.1$	$\sigma = 0.2$	$\sigma = 0$	$\sigma = 0.1$	$\sigma = 0.2$
Tikhonov [1]	21.50/31 (0.1s)	21.17/34 (0.1s)	20.35/39 (0.1s)	34.11/241 (11s)	33.32/251 (11s)	31.53/266 (11s)
PD-TV [1]	24.74/4k (21s)	23.92/3.8k (20s)	22.37/3.5k (19s)	37.75/6k (204s)	36.04/3k (102s)	34.50/2k (68s)
DIP [2]	22.81/1.2k (44s)	20.21/112 (4s)	19.43/45 (2s)	36.1/7k (1.3 hr)	33.4/7k (1.3 hr)	28.00/7k (1.3 hr)
DIP enhanced	25.50/1.4k (54s)	24.00/402 (15s)	**23.71**/349 (13s)	38.44/4k (0.8 hr)	34.6/4.6k (0.9 hr)	32.66/2.6k (0.5 hr)
PnP [1]	25.57/1.7k (14s)	24.54/1.2k (9.6s)	23.48/1.5k (12s)	N/A	N/A	N/A
IntraSeismic	**26.34**/1.5k (7s)	**24.71**/457 (2s)	23.25/286 (1s)	**40.8**/600 (28s)	**36.57**/262 (13s)	**34.59**/307 (15s)

Note. SNR/Iterations (total time in seconds or hours) are shown in each entry, and **bold** is used to indicate the best-performing algorithm for any combination of model and noise. Benchmark methods' results are based on the code from [1] Romero, Corrales, et al. (2022) and [2] Ravasi, Romero, et al. (2023).

Modeling Operator: In the applications presented in subsequent sections, we utilize the pre-stack (5), post-stack (9), and 4D post-stack seismic modeling operators. Note that we refer as 4D post-stack seismic modeling operator to the block diagonal matrix that contains two post-stack modeling operators as shown in Equation 11.

Optimizer: For all applications, we utilize the Adam optimizer (Kingma & Ba, 2014) with a learning rate of 10^{-3}. We employ a single batch approach, processing all input coordinates simultaneously, to solve for the IntraSeismic parameters derived from the MLP and hash encoding tables.

Implementation details: The IntraSeismic framework is fully implemented in PyTorch 2.0.1, and all experiments are conducted on an AMD EPYC 7713 64-Core Processor equipped with a single NVIDIA TESLA A100. The modeling operator is implemented and wrapped into PyTorch using the PyLops library (Ravasi & Vasconcelos, 2020).

4. Experiments

This section evaluates IntraSeismic's effectiveness and performance across various scenarios. For each data set, we train a specific IntraSeismic framework. We present results for post-stack seismic inversion on 2D and 3D synthetic data with varying noise levels, followed by a field 3D example. We then showcase IntraSeismic's versatility for joint inversion of multiple elastic properties using a synthetic pre-stack seismic data set. Finally, we demonstrate IntraSeismic's application to 4D seismic data through the inversion of 4D synthetic and field seismic data sets. In each case, we compare IntraSeismic's outcomes against state-of-the-art methods reported in the literature.

4.1. Post-Stack Seismic Inversion

We apply IntraSeismic to both 2D and 3D synthetic post-stack seismic data sets, incorporating band-passed Gaussian noise at varying standard deviations: noise-free ($\sigma = 0$), $\sigma = 0.1$, and $\sigma = 0.2$. It is worth noting that the seismic data set is scaled from -1 to 1. In Table 1, we report the Signal-to-Noise Ratio (SNR) of the obtained solution, the number of iterations needed to achieve such a result, and the total processing time for IntraSeismic and benchmark methods. In the subsequent subsections, we illustrate the results when using a moderate noise level ($\sigma = 0.1$), which is reflective of the usual noise levels encountered in field data. Figures 3a and 5a display the corresponding data for the Marmousi and SEAM models. In both cases, the seismic data is modeled using a Ricker wavelet (Ricker, 1943) with a peak frequency of 15 Hz, and the background models are smoothed versions of the original acoustic impedance models (Figures 3b and 5b).

The IntraSeismic result on synthetic data is benchmarked with two variational approaches, Tikhonov regularization (the standard method used in industry) and TV regularization using the Primal-Dual solver (Ravasi & Birnie, 2022) (referred to from here onwards as PD-TV). Additionally, we compare IntraSeismic with the state-of-the-art hybrid methods proposed in the literature for post-stack seismic inversion, namely the DIP (Lipari et al., 2021), as well as Plug-and-Play priors with deep denoisers (Romero, Corrales, et al., 2022). For the PnP results, we utilized the code published in (Romero, Corrales, et al., 2022), which employs the DRUNet denoiser

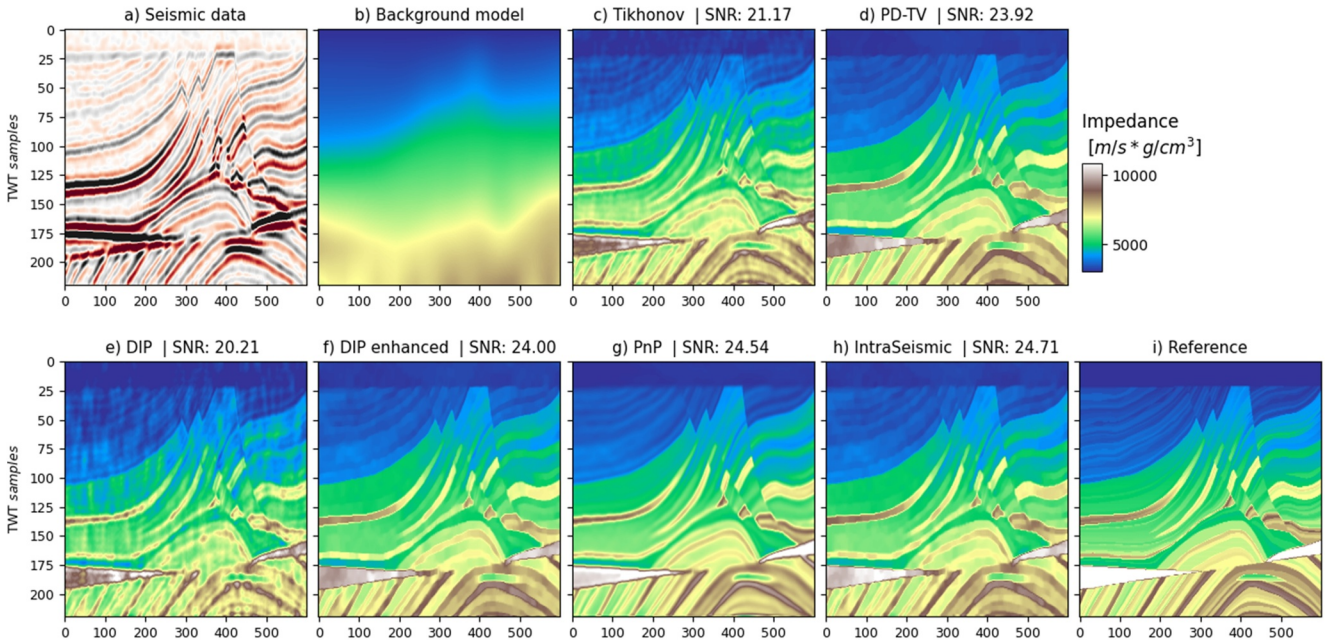

Figure 3. Inversion of the synthetic 2D Marmousi data set with a noise level of $\sigma = 0.1$: (a) seismic data, (b) background model, (c) Tikhonov regularization, (d) TV-regularization using the Primal-Dual solver, (e) Deep Image Prior (DIP), (f) DIP with additional priors, (g) PnP, (h) IntraSeismic, and (i) ground truth.

(Zhang et al., 2022) within a Primal-Dual solver. This approach has been shown to achieve state-of-the-art outcomes in 2D post-stack seismic inversion. As of the publication date of our paper, we are not aware of any published implementation of PnP for 3D data. Consequently, we do not include a comparison with PnP in our 3D synthetic and field data experiments. In the case of DIP (Ravasi, Luiken, et al., 2023), showed that the originally proposed method becomes sub-optimal in the presence of noise in post-stack seismic inversion. This limitation may stem from the absence of prior information that guides the inversion toward geologically consistent solutions. In our study, we further modify DIP by incorporating the same regularization terms as those used in IntraSeismic (see Equation 12), and we refer to it as DIP enhanced. We believe that this facilitates a more equitable comparison between the DIP and IntraSeismic methods, where their main difference lies in the parameterization of the acoustic impedance model (i.e., a CNN that warps a noise vector into the sought-after solution in DIP, and an MLP that transforms coordinates into values of the solution in IntraSeismic). Finally, we decided not to provide any comparison with state-of-the-art supervised learning approaches as that would introduce additional factors (e.g., size of the training data set) that greatly affect the quality of the final solution.

4.1.1. Marmousi Model

The Marmousi model (Brougois et al., 1990) is a synthetically created, realistic 2D subsurface velocity model that emulates complex geological structures with sharp velocity contrasts (see Figure 3i). The Marmousi model is one the most widely used models in geophysics, thereby serving as a benchmark for various seismic imaging and inversion algorithms. Figure 3c–3f) illustrate the inversion results for the Marmousi data set at a noise level of $\sigma = 0.1$, comparing standard variational methods, hybrid algorithms, and IntraSeismic. IntraSeismic retrieves a high-resolution acoustic impedance image of the Marmousi model, where discontinuities and layer contrasts are clearly defined. Like PD-TV, IntraSeismic struggles to capture the layer with the highest impedance, a detail that the PnP method captures more effectively, as shown in Figure 3g). This difficulty in reproducing precise contrasts is a recognized limitation of TV regularization. See a detailed profile view of the different results in Figure E1 in Supporting Information S1.

Figure 4 (left) illustrates the evolution of the loss function over iterations. The curve exhibits a sharp decrease in the first 50 iterations, followed by a near-constant behavior, indicating that the network is rapidly learning the dominant features of the Marmousi model. When looking at the SNR evolution through iterations (Figure 4 (right)), we observe a similar trend: a rapid increase within the first 200 iterations, followed by a plateau,

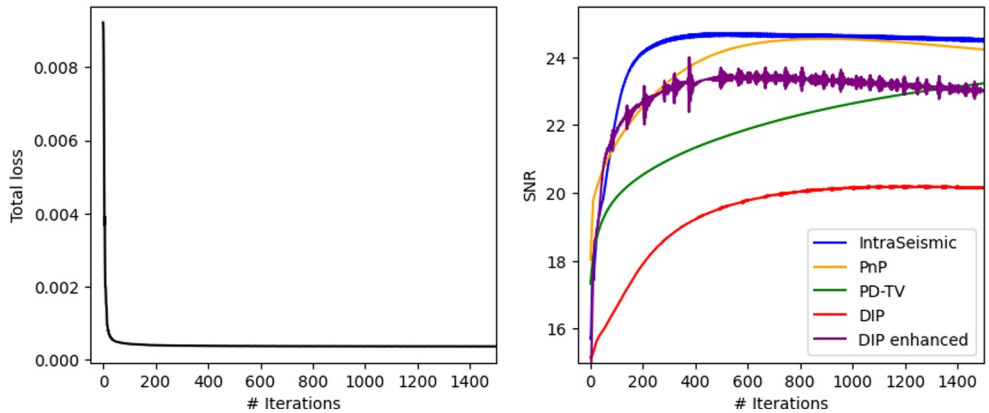

Figure 4. Loss (left) and SNR (right) evolution through iterations for IntraSeismic in the inversion of the Marmousi data. The SNR plot also includes the SNR corresponding to each of the benchmark methods.

demonstrating the fastest convergence rate compared to benchmark methods. Table 1 highlights that IntraSeismic achieves the highest SNR for the Marmousi model under both noise-free conditions and noisy data with a standard deviation of 0.1. However, for the highest noise level (standard deviation of 0.2), the DIP-enhanced method achieves a slightly better SNR.

4.1.2. SEAM Model

For our 3D example, we consider a volume of size 180 × 180 × 180, extracted from the SEAM Phase I velocity model created by the SEG Advanced Modeling Consortium (Fehler & Keliher, 2011). The SEAM model showcases realistic geological heterogeneities and discontinuities across all three spatial dimensions and exhibits high contrasts between some of its layers (Figure 5h). Evidently, the IntraSeismic method (Figure 5g) produces the solution with the highest SNR, leading to a more precise 3D reconstruction of the SEAM model. Similar to the Marmousi example, IntraSeismic struggled to accurately capture the impedance values of the model's highest impedance layer, a feature that shares with PD-TV. See a detailed profile view of the results in Figure E2 in Supporting Information S1.

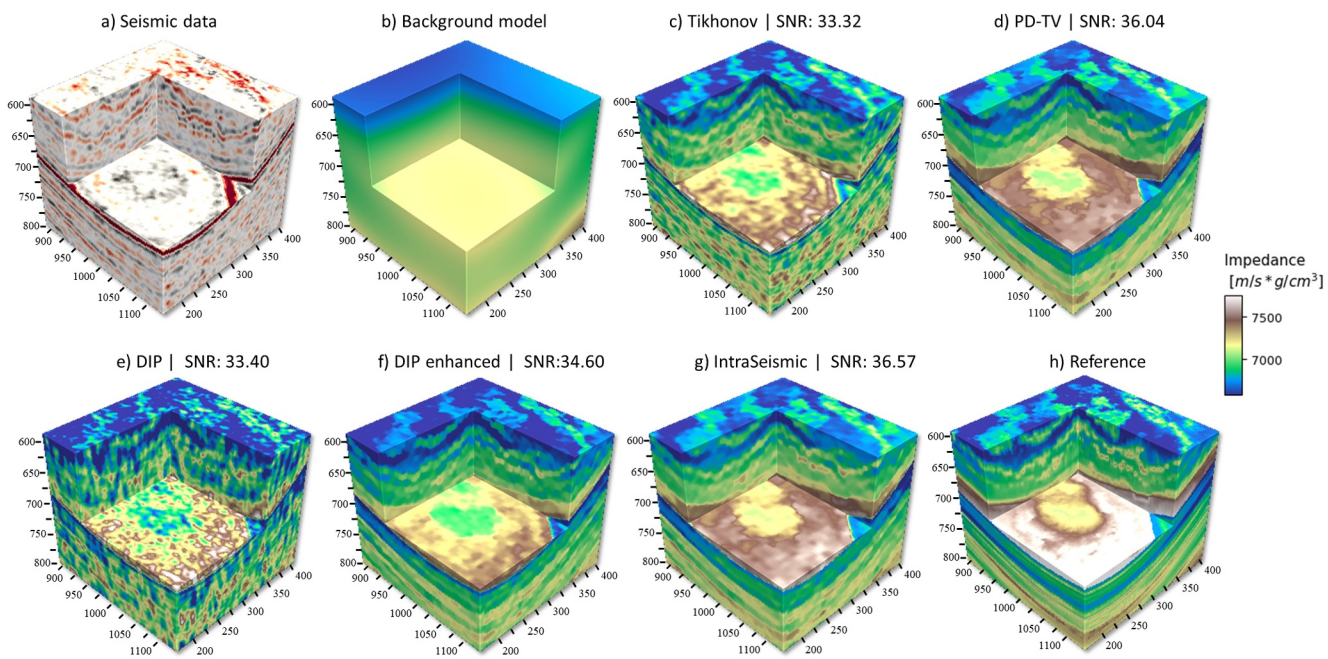

Figure 5. Inversion of the synthetic 3D SEAM data set: (a) seismic data, (b) background model, (c) Tikhonov regularization, (d) TV-regularization using the Primal-Dual solver, (e) Deep Image Prior (DIP), (f) DIP with additional priors, (g) IntraSeismic, and (h) ground truth.

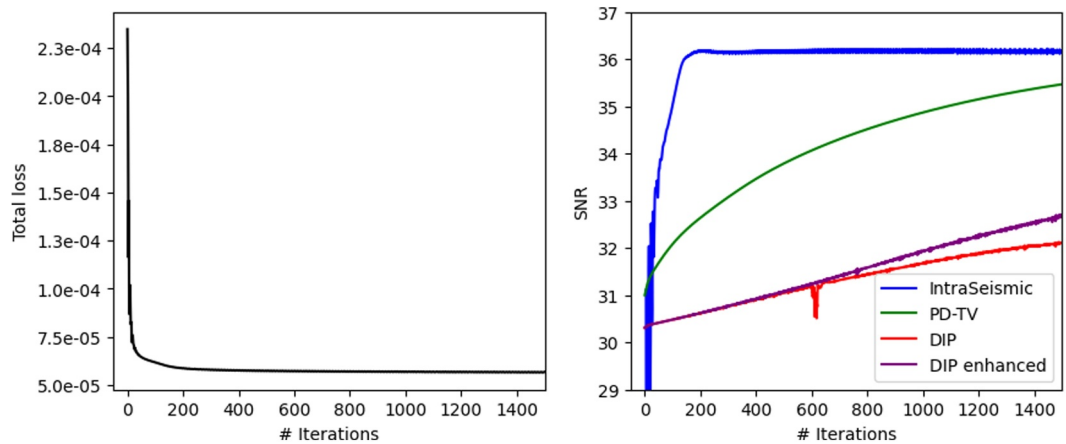

Figure 6. Loss (left) and SNR (right) evolution through iterations for IntraSeismic in the inversion of the SEAM data. The SNR plot also includes the SNR corresponding to the benchmark methods.

As demonstrated in Table 1, IntraSeismic achieves the highest SNR for all noise levels for the SEAM data set. Additionally, IntraSeismic consistently required fewer than 400 iterations to converge across all evaluated noise scenarios, significantly outpacing the benchmark methods, which required more than 2,000 iterations to achieve their own best results. This is also illustrated in Figure 6 (right), where the SNR evolution over iterations is shown for IntraSeismic and the benchmark methods in the case of SEAM noisy data ($\sigma = 0.1$) inversion. Similar to the Marmousi example, a steep decrease of the IntraSeismic loss is observed in the first 100 iterations followed by a plateau –Figure 6 (left).

4.1.3. Field Data: Sleipner Data Set (Static)

The Sleipner data set, a publicly accessible 4D seismic data set, comprises one baseline seismic survey acquired in 1994 and six subsequent monitor surveys acquired in 1999, 2001, 2004, 2006, 2008, and 2010. These surveys are being used to monitor the continuous injection of CO_2 into the saline aquifer of the Middle Miocene/Early Pliocene Utsira Formation (Chadwick et al., 2010). In the current example, we use only the 2001 full-stack seismic data set as we are performing static post-stack seismic inversion. We use a subvolume of size $300 \times 300 \times 250$ (Figure 7a), which exhibits a predominantly horizontal geology disrupted by strong contrast values in the CO_2 reservoir. In order to be able to invert this data set, we extract a statistical wavelet directly from the full-stack data and create a background model (Figure 7b) with the help of well logs acquired in a vertical well. For more details, we refer the reader to (Romero et al., 2023). Figure 7 shows the inversion results for the benchmark methods and IntraSeismic. In this case, IntraSeismic and PD-TV produce results of superior quality compared to the other methods. IntraSeismic shows smoother transitions in the horizontal direction (a sought-after characteristic in geology) and heightened resolution in the vertical direction that accentuates the layer contrasts. See the detailed profile view of the results in Figure E3 in Supporting Information S1. Figure 8 (left) illustrates the loss function for IntraSeismic in the inversion of the Sleipner data set, and (right) the relative SNR computed using the inversion at 500 iterations as a reference. Notably, after 400 iterations, the SNR of the model output reaches relative stability, oscillating around an SNR of 37. This lack of significant increase is interpreted as the convergence point.

4.2. Pre-Stack Seismic Inversion

As mentioned in 3.2, IntraSeismic can be seamlessly extended to directly invert pre-stack seismic data, simultaneously retrieving elastic properties such as P and S-waves velocity, and density. To showcase the applicability of IntraSeismic to pre-stack seismic inversion, we use a portion of the synthetic elastic Marmousi model (Martin et al., 2006), shown in Figures 9c–9c. Figures 9d–9f illustrate the background models used as starting guesses for the inversion, which are obtained by smoothing the corresponding ground truth models. Figures 9g–9i present three of the 21 computed common-angle gathers (i.e., pre-stack data at a fixed angle).

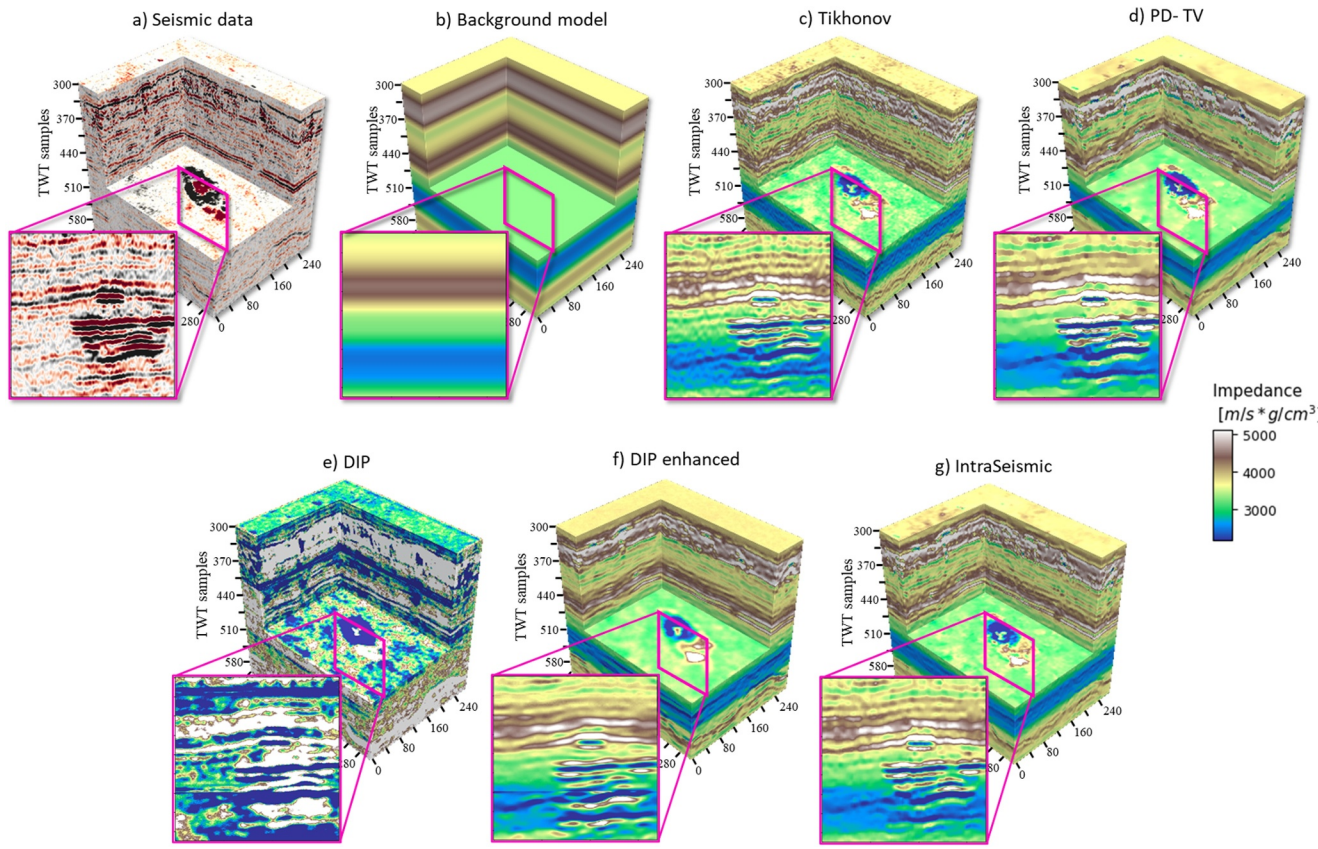

Figure 7. Inversion of Sleipner data set using IntraSeismic and benchmark methods: (a) seismic data, (b) background model, (c) Tikhonov regularization, (d) TV-regularization using the Primal-Dual solver, (e) Deep Image Prior (DIP), (f) DIP with additional priors, and (g) IntraSeismic.

Figure 10 presents the results of pre-stack inversion using a single IntraSeismic non-linear mapping module (as explained in 3.2.1) to produce P-wave velocity, S-wave velocity, and density. This approach shows a reasonable reconstruction of P and S-wave velocity models, although the latter displays a lower SNR. The estimation of the density model, on the other hand, appears notably noisier than the other two; note, however, that the density estimate achieves a higher SNR, which is attributed to the limited value range (2,000–2,500 kg/m^3), resulting in a

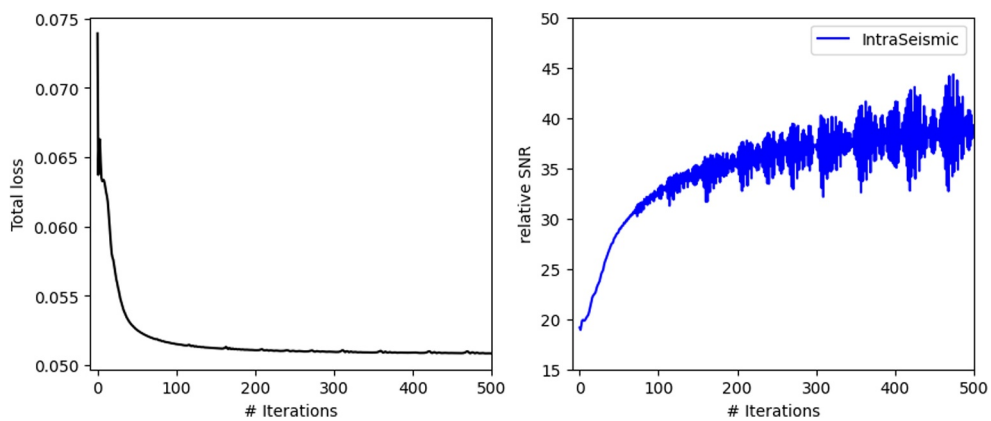

Figure 8. Loss (left) and relative SNR (right) evolution through iterations for IntraSeismic in the inversion of the Sleipner data. The reference used for the relative SNR calculation corresponds to the inverted volume at iteration 500 (SNR at the 500th iteration is not shown in the plot).

10.1029/2024JH000275

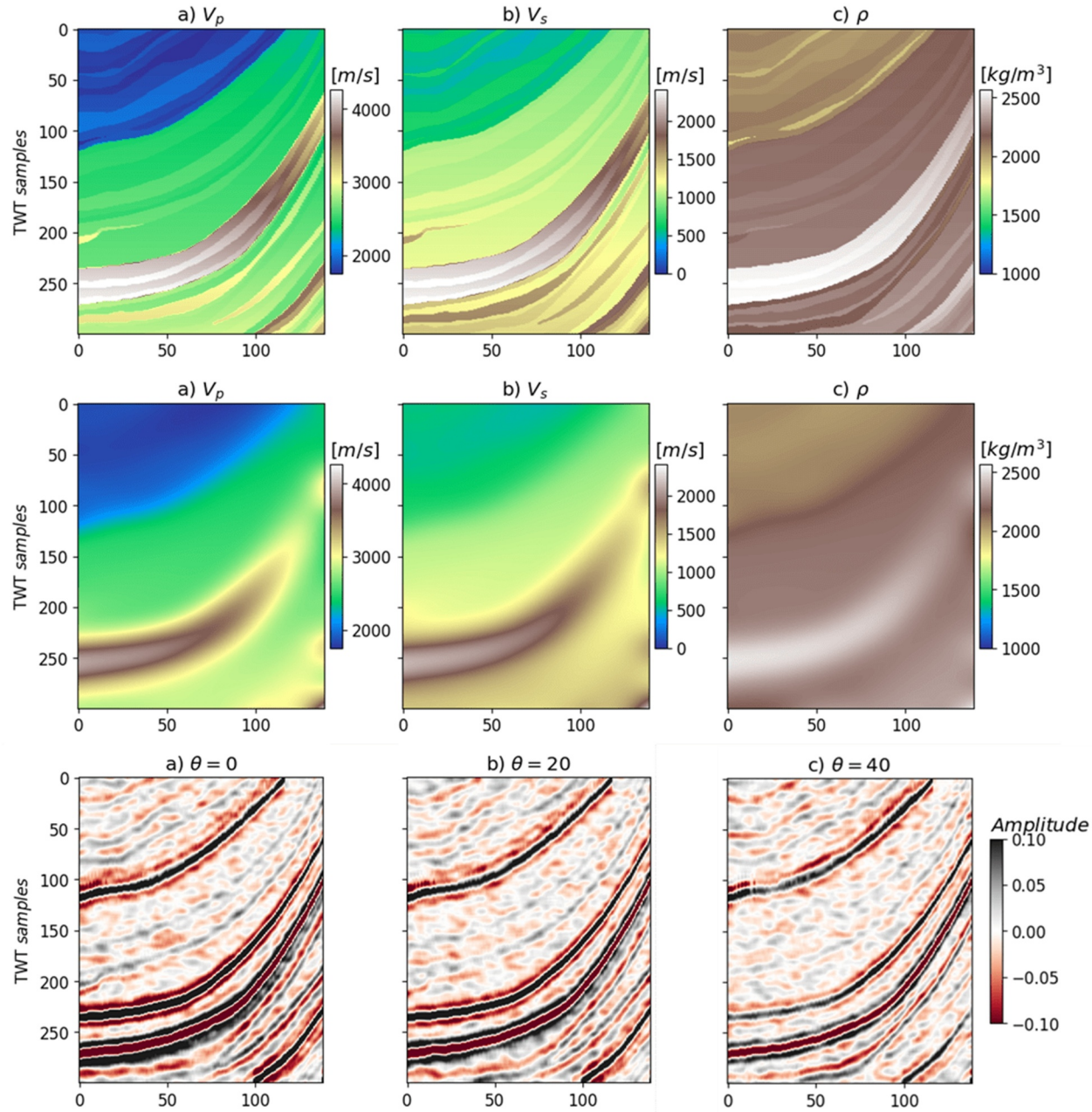

Figure 9. Elastic Marmousi model: (a–c) ground truth parameters P-wave velocity $\mathbf{V_p}$, S-wave velocity $\mathbf{V_s}$ and density ρ, and (d–f) background models. (g–i) modeled pre-stack seismic data for angles $\theta = 0$, $\theta = 20$, and $\theta = 40$.

naturally lower TV term compared to other inverted properties. Conversely, Figure 11 depicts the results of pre-stack inversion using three distinct non-linear mapping modules frameworks that are simultaneously optimized to produce P-wave velocity, S-wave velocity, and density (as explained in 3.2.2). In this case, the use of three independent mappings yields a more effective reconstruction of the P and S-wave velocity models. This is evident from their visual alignment with the ground truth models (Figures 9a–9c) and improved SNRs compared to those of the first approach. However, similar to the first method, the density estimate is less accurate compared to P and S-wave velocities, resembling a lower-resolution version of the ground truth model. This issue is well-known in pre-stack seismic inversion and is not specific to IntraSeismic, owing to the limited sensitivity of pre-stack seismic data to density variations (Downton, 2005). Consequently, modifying the regularization weights for each parameter inevitably improves one model at the cost of the others.

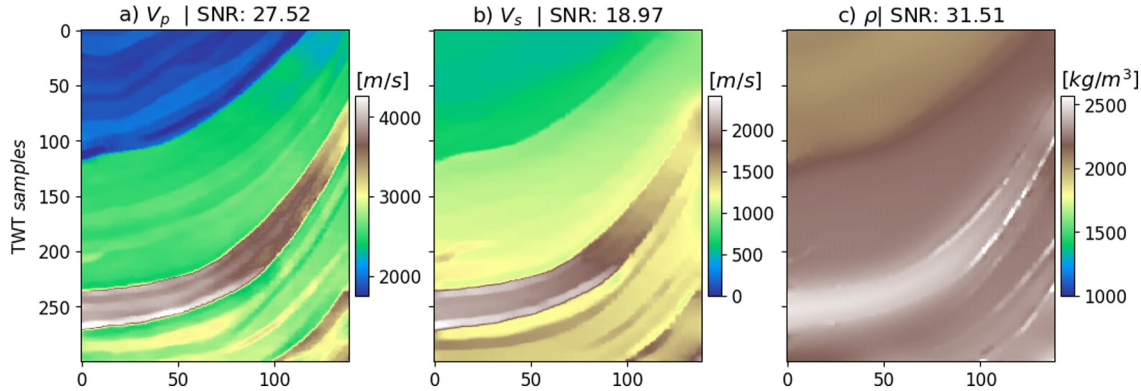

Figure 10. Pre-stack inversion results of a portion of the elastic Marmousi model a single IntraSeismic non-linear mapping module: (a) P-wave velocity $\mathbf{V_p}$, (b) S-wave velocity $\mathbf{V_s}$, and (c) density ρ.

Figure 13 illustrates the SNR evolution over iterations for each model in both IntraSeismic implementations with shared and independent non-linear mapping modules for pre-stack inversion. Both methods demonstrate swift convergence for the three models, with the SNR peaks occurring nearly simultaneously and exhibiting stable behavior after convergence. Additionally, Figure 12 shows the benchmark pre-stack inversion approach that uses isotropic TV regularization for each inverted property using the PD-TV algorithm (Ravasi, Romero, et al., 2023). Compared to this benchmark, IntraSeismic pre-stack implementations are superior in terms of inverted models quality.

4.3. 4D Post-Stack Seismic Inversion

4.3.1. Synthetic 4D VTI Hess Data Set

We first consider a time-lapse version of the VTI Hess model (Romero, Luiken, & Ravasi, 2022). The baseline model alongside the modeled 4D difference are displayed in Figures 14a and 14b. For the post-stack seismic modeling operator, we employ a Ricker wavelet with a peak frequency of 15 Hz, accompanied by filtered Gaussian noise with $\sigma = 0.1$ (Figures 14c and 14d). The inversion products from a state-of-the-art variational-based 4D simultaneous post-stack inversion algorithm, as described in (Romero, Luiken, & Ravasi, 2022), are illustrated in Figures 14e and 14f. This method incorporates TV regularization in both the baseline and monitor models, as well as in their differences and solves the associated objective function via the PD-TV algorithm. Notably, the inversion results obtained by 4D-IntraSeismic reveal a higher resolution baseline impedance model (Figure 14g), with an improved SNR in comparison to that of PD-TV approach (Figure 14e). Furthermore, the time-lapse changes estimated by 4D-IntraSeismic (Figure 14h) present minimal noise associated with the non-repeatable nature of the added noise, significantly enhancing our ability (and, possibly, also that of subsequent automated detection procedures) to identify true time-lapse changes in the subsurface. In both cases, it is however

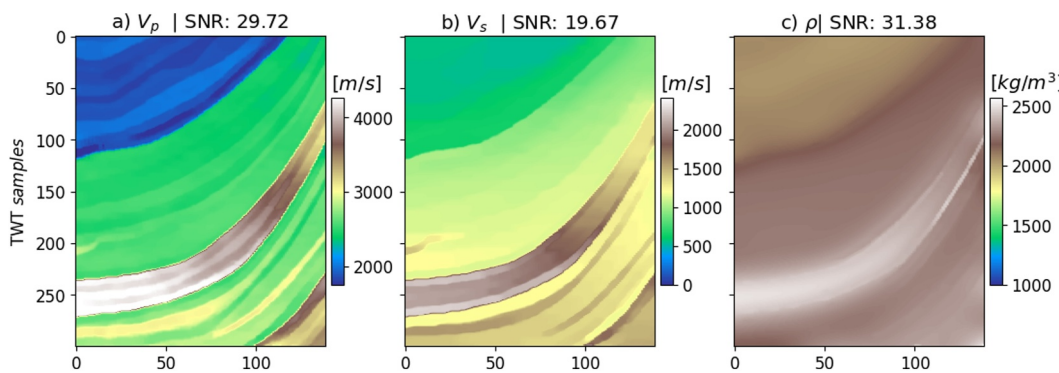

Figure 11. Pre-stack inversion results of a portion of the elastic Marmousi model using IntraSeismic with three independent non-linear mapping modules: (a) P-wave velocity $\mathbf{V_p}$, (b) S-wave velocity $\mathbf{V_s}$, and (c) density ρ.

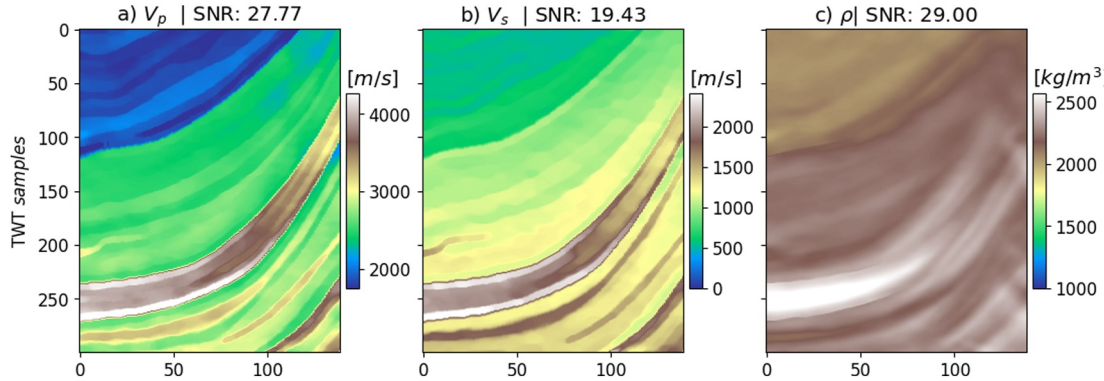

Figure 12. Pre-stack inversion results of a portion of the elastic Marmousi model using PD-TV: (a) P-wave velocity $\mathbf{V_p}$, (b) S-wave velocity $\mathbf{V_s}$, and (c) density ρ.

worth mentioning that the value of the time-lapse changes is slightly underestimated. This underestimation can be attributed to the inherent loss of contrast in TV-based regularization. Figure 15 displays the SNR evolution for the inverted baseline model over iterations using both 4D-IntraSeismic and PD-TV. 4D-IntraSeismic demonstrates faster convergence, reaching an SNR of 35.10 dB in approximately 2,000 iterations. In contrast, PD-TV requires over 5,000 iterations to achieve a comparable SNR of 34.94 dB.

4.3.2. Field Data: Sleipner Data Set (Dynamic)

For our dynamic study (4D post-stack seismic inversion), we select one representative section from the 1994 and 2001 Sleipner full-stack seismic volumes passing through the most notable 4D effect (Figures 16a and 16b) and evaluate the effectiveness of 4D-IntraSeismic when dealing with field data. The results of the benchmark PD-TV inversion algorithm are displayed in Figures 16c and 16d), while those from 4D-IntraSeismic are presented in Figures 16e and 16f. As far as the baseline model is concerned, the acoustic impedance model obtained from 4D-IntraSeismic features enhanced vertical resolution and improved horizontal continuity for most of the layers compared to the PD-TV counterpart. Similarly, the 4D difference obtained by 4D-IntraSeismic more distinctly delineates the real time-lapse changes, notably highlighting the host layers of the injected CO_2.

5. Additional Features and Discussion

Building upon the core framework of IntraSeismic described thus far, we identify several promising areas of research that could benefit from the utilization of INRs within IntraSeismic. Here, we provide a preliminary evaluation of their potential.

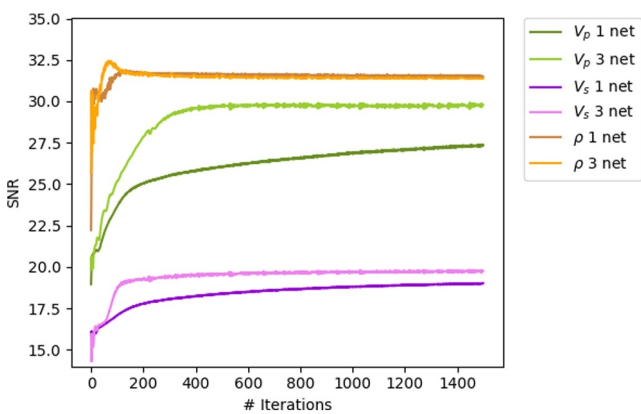

Figure 13. SNR evolution through iterations for each elastic parameter $\mathbf{V_p}$, $\mathbf{V_s}$, and ρ using single shared IntraSeismic non-linear mapping module (1 net), and three independent IntraSeismic non-linear mapping modules (3 net).

5.1. Uncertainty Quantification

Uncertainty quantification is pivotal in any seismic inversion process given the non-uniqueness of the seismic inverse problem, the inherent complexity and variability of the Earth's subsurface, and the previously discussed limitations of the observed data. As such, UQ offers insight into the range of possible subsurface models that can equally fit the observed data. This knowledge is instrumental for informed decision-making in scenarios with significant financial and environmental implications (R. C. Smith, 2013). Furthermore, understanding the uncertainties associated with a seismic inversion product can guide subsequent data acquisition campaigns to refine results and provide a clearer picture of result reliability and associated risks. When a neural network is involved directly (via supervised learning) or indirectly (as a regularizer or preconditioner) in the solution of the seismic inverse problem, additional uncertainty is introduced in the process. Among other techniques to quantify such an uncertainty component, Monte Carlo Dropout (MCD) has been shown to be an effective and easy-to-implement method to quantify the so-called epistemic uncertainty associated with

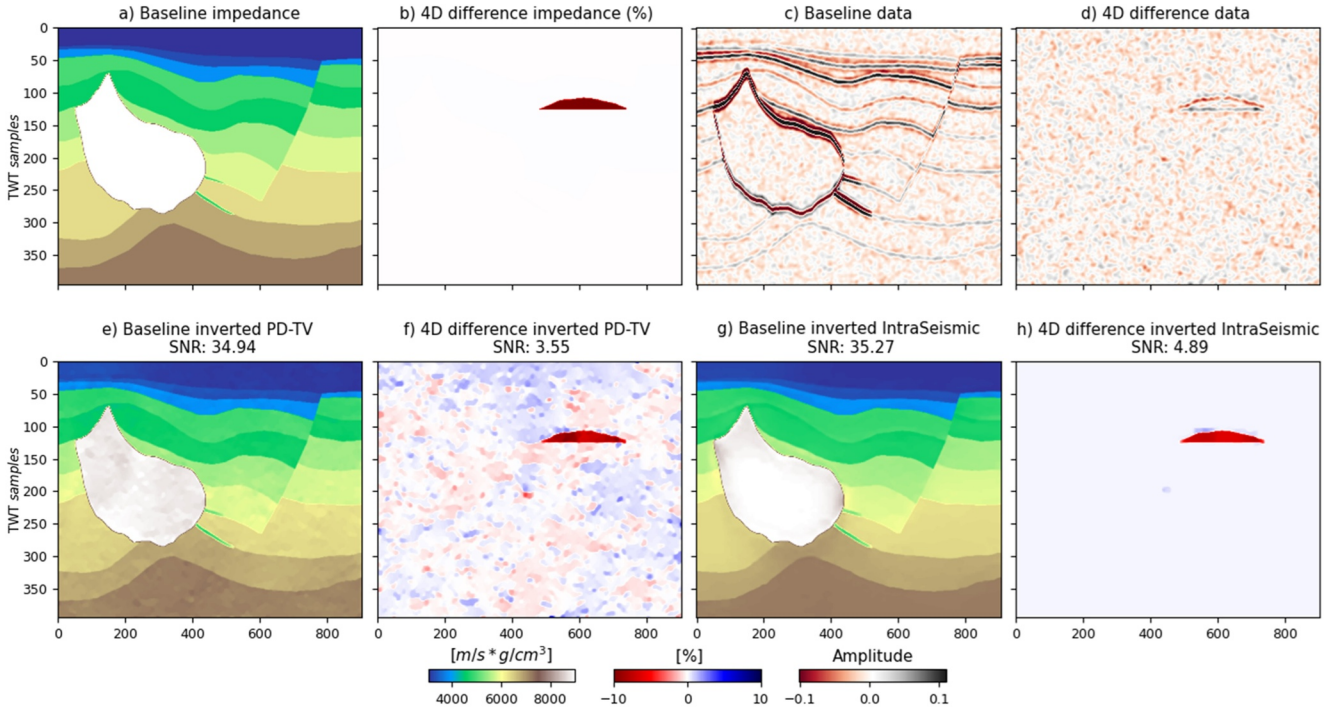

Figure 14. Inversion results of 4D-IntraSeismic applied to the Hess VTI Data set: (a) Reference baseline acoustic impedance model; (b) reference 4D impedance difference; (c) Modeled post-stack seismic based on the reference model in (a); (d) 4D seismic difference; (e–f) Baseline impedance model and 4D impedance difference inversion using the PD-TV algorithm; (g–h) baseline impedance model and 4D impedance difference inversion using 4D-IntraSeismic.

network (Gal & Ghahramani, 2016). By retaining the dropout layers during the inference phase, rather than just during training, and performing multiple evaluations of the network with different neurons "dropped out" each time, one can obtain samples of an approximate posterior distribution (Kendall & Gal, 2017). We propose to add dropout layers to IntraSeismic's MLP and to perform MCD sampling once the optimization process is completed. The proposed technique is applied to the Marmousi model. More specifically, in this case, we apply dropout to both of the layers of the MLP (Figure 1) with a dropout probability of 0.2, and we compute a total of 100 realizations, which are used to evaluate sample statistics (e.g., sample mean and standard deviation). Figure 17 corresponds to the obtained standard deviation divided by the mean of the Marmousi model parameters that shows the IntraSeismic's confidence levels and highlights areas in the model with potential ambiguity in the solution. The layers with higher contrast of impedance with the surroundings exhibit the highest uncertainty, possibly due to TV regularization, which might lead to a diminished contrast. Despite the promising results demonstrated by MCD and its robustness compared to other UQ techniques (Vasconcelos et al., 2023), UQ within the realm of INRs remains a vibrant area of research within the computer vision community (Goli et al., 2023; Shen et al., 2022; Vasconcelos et al., 2023). The integration and adaptation of these UQ methodologies into the IntraSeismic framework is subject of ongoing research.

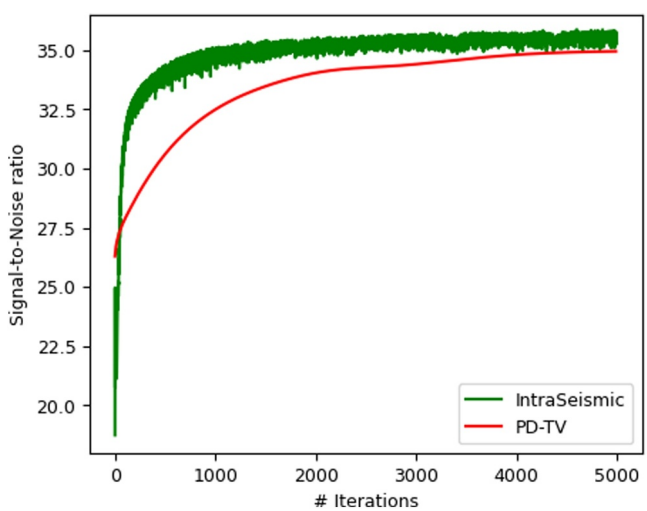

Figure 15. SNR evolution for the Hess VTI baseline impedance model using 4D-IntraSeismic and PD-TV.

5.2. Adding Hard-Constraints

Well-log data provide the closest approximation to the ground truth subsurface parameters that we aim to estimate via seismic inversion. As such, they can serve as critical anchor points, ensuring that the seismic inversion results are consistent with real-world measurements at specific locations. One way to incorporate well-log data in the seismic inversion process is by integrating it directly into the original optimization framework. This can be achieved by introducing a soft constraint to the optimization problem as formulated in

10.1029/2024JH000275

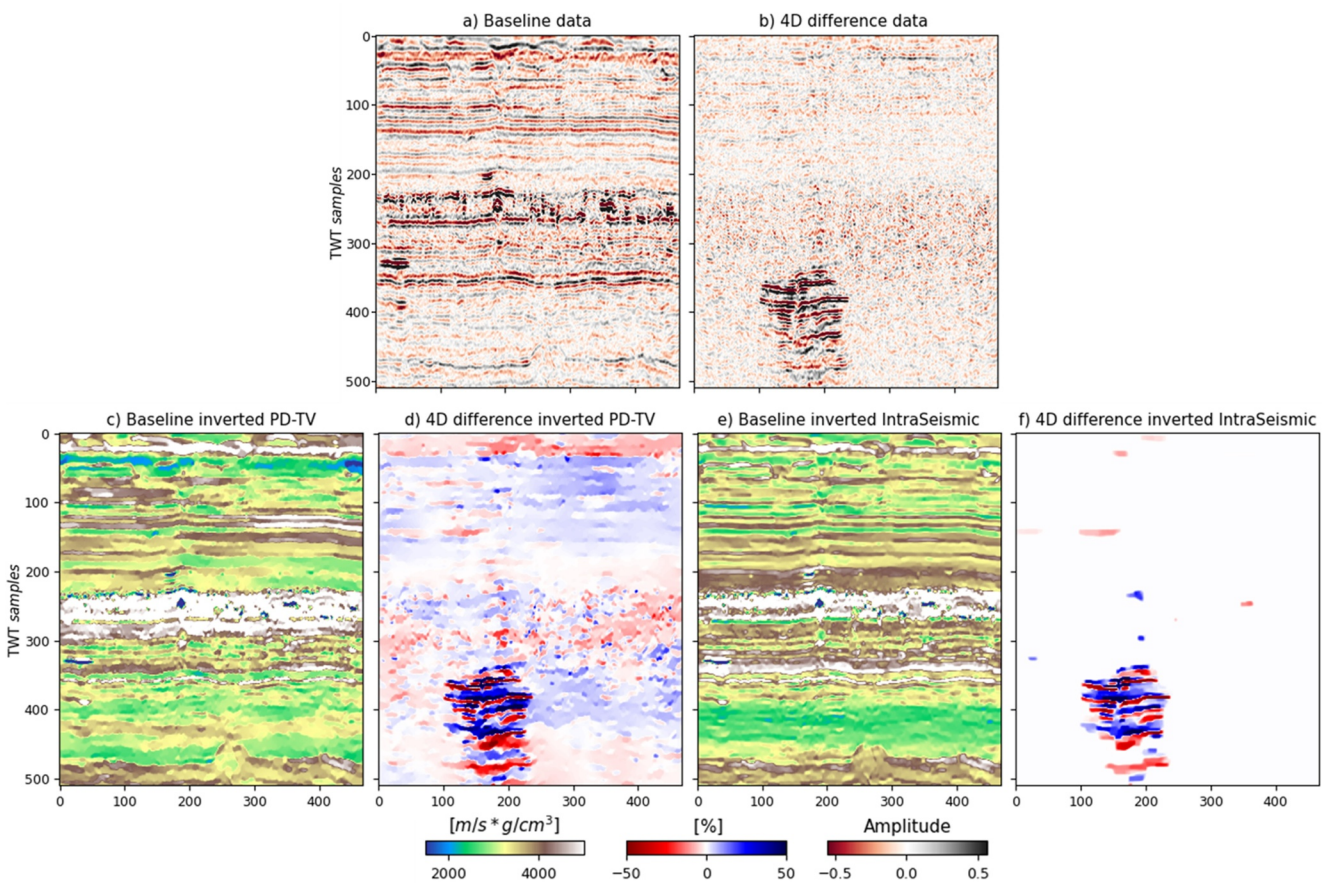

Figure 16. Inversion results of 4D-IntraSeismic applied to the Sleipner field data set: (a) Baseline post-stack migrated seismic data; (b) 4D seismic difference, (c–d) Baseline impedance model and 4D impedance difference inversion using the PD-TV algorithm; (e–f) baseline impedance model and 4D impedance difference inversion using 4D-IntraSeismic.

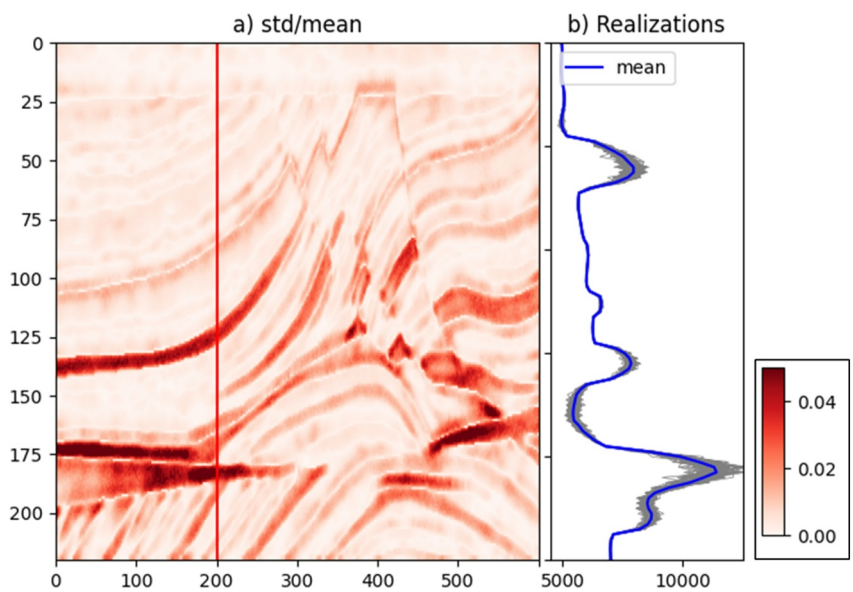

Figure 17. Monte Carlo Dropout uncertainty quantification result for Marmousi model: (a) std/mean, the red line indicates the extracted column shown in (b).

Equation 10. Specifically, the term $\gamma\|\boldsymbol{m}_i - \boldsymbol{m}_{\text{well}}\|_2^2$ can be added, where γ is a weighting factor that balances the influence of the well-log data, $\boldsymbol{m}_i$ represents the model parameters at the well position, and $\boldsymbol{m}_{\text{well}}$ denotes the measurements from the well-log. This addition ensures that the inversion solution aligns more closely with the well-log observations. An alternative for incorporating well-log data into the seismic inversion process involves the application of a hard constraint, which enforces an exact match between the impedance model and the well-log data ($\boldsymbol{m}_i = \boldsymbol{m}_{\text{well}}$). This approach is particularly advantageous in instances of highly noisy data where the integrity of well data is prioritized or in scenarios with numerous wells within a development field, where the objective is to construct a robust model that accurately reflects all available well data. In IntraSeismic, the integration of well data can be naturally achieved by redefining the MLP output as follows (Schiassi et al., 2020):

$$\boldsymbol{m} = (\boldsymbol{x} - \boldsymbol{x}_{\text{well}})\Delta\boldsymbol{m}_{\Theta} + \boldsymbol{m}_{\text{well}} \tag{15}$$

where $\boldsymbol{x}$ represents the coordinate vector, while $\boldsymbol{x}_{\text{well}}$ and $\boldsymbol{m}_{\text{well}}$ denote the coordinates and values of the well-log data, respectively. The term $\Delta\boldsymbol{m}_{\Theta}$ corresponds to the output of the IntraSeismic MLP. Within this framework, the MLP output ensures compliance with the hard constraint and acts as an update to the well data away from its position. In case there is more than one well available, Equation 15 can be further modified to include a weighted interpolation to compute the distance of a given point to the wells.

We implemented the IntraSeismic framework with well-log as a hard constraint in a single slice of the Sleipner data set passing through a vertical well. As such, the solution is naturally forced to match the available acoustic impedance well-log at the well location. Figures 18a and 18b display the IntraSeismic MLP output $\boldsymbol{m}_{\Theta}$ and the final inverted Sleipner impedance model incorporating well-log data as a hard constraint, respectively. Figure 18c) compares the well-log with the corresponding inverted trace obtained using IntraSeismic without well information (unconstrained), with well-log data as a soft constraint, and as a hard constraint. As anticipated, results with a hard constraint perfectly match the well-log, whereas the unconstrained inversion deviates significantly from the well-log's high-frequency details. The soft-constrained inversion lies between the unconstrained and hard-constrained solutions.

5.3. Irregular Data Access and Data Compression

Geoscientists are constantly tasked to analyze vast amounts of seismic data, a process usually referred to as seismic interpretation (Herron, 2011). As such, the property models produced by different seismic inversion algorithms are commonly visualized along different axes (i.e., inline, crossline, time/depth) or along irregular surfaces corresponding to key geological horizons. Conventional seismic interpretation software packages perform such extraction procedures operating directly with data stored on fast-access file storage systems or on local memory when the data size allows it.

However, a user must select upfront the layout of the data, placing the most commonly accessed direction over the fast axis and the least commonly accessed direction over the slow one or replicating the same information over multiple files with different layouts. In order to reduce the amount of I/O, the seismic industry has recently placed tremendous focus on compression algorithms, with the popular ZFP data format (Lindstrom, 2014) being widely adopted in both proprietary and open-source data formats (e.g., MDIO (Sansal et al., 2023)). A second by-product of the IntraSeismic framework is represented by the coordinate-based parameterization of the sought-after acoustic impedance model. As such, the cost of accessing the model values at N (possibly random) coordinates is independent of the location and order of such points. We believe that this unique feature of IntraSeismic could revolutionize how seismic interpretation software packages store and access seismic volumes.

Moreover, given that the complete knowledge of the acoustic impedance model is encapsulated within the learned hash tables and the parameters of the MLP, the IntraSeismic framework can be considered an effective data compression tool. In this scenario, INRs convert the challenge of data compression into one of parameter or model compression, a subject that is currently a focal point of research within the image compression domain in the computer vision community (Dupont et al., 2021). The SEAM model, illustrated in Figure 5, comprises of 5.83 million data points, yet the IntraSeismic framework can represent it with only 1.16 million parameters. This yields a compression ratio of approximately 5. In contrast, the ZFP compression algorithm achieves a compression ratio of approximately 15 for the SEAM model, with an error margin of 0.1%. A significant factor in the high

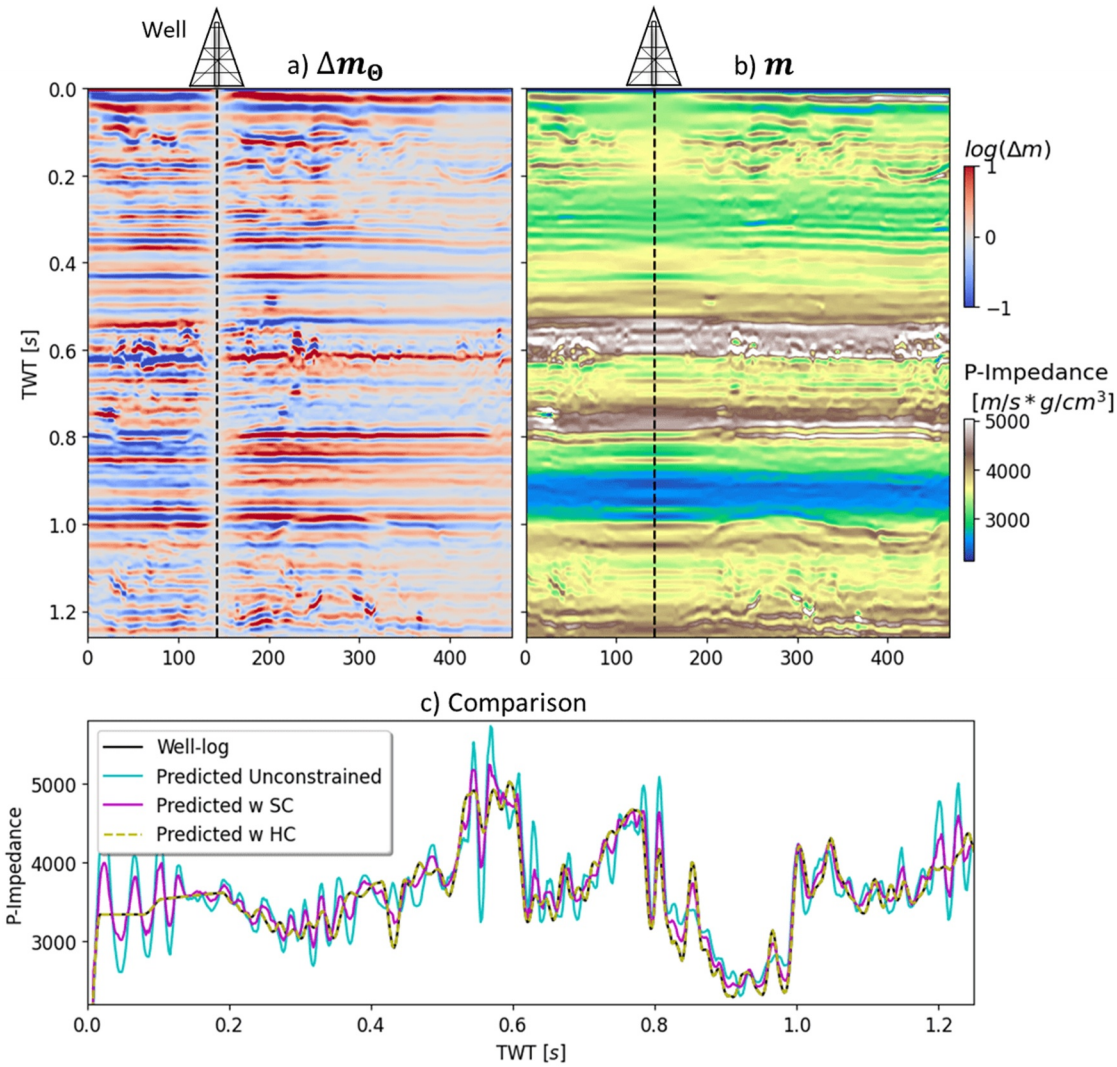

Figure 18. IntraSeismic hard-constrained inversion of Sleipner data set: (a) multi-layer perceptron output Δm_Θ, and (b) final estimated acoustic impedance model. (c) shows the comparison at the well location of the unconstrained, soft-constrained, and hard-constrained IntraSeismic inversions.

compression efficiency of ZFP can be attributed to its quantization step performed prior to storing the compressed data. The compression ratio of IntraSeismic could potentially be enhanced through the quantization of the hash table and MLP (Dupont et al., 2021; Strümpler et al., 2022), more specifically, by optimizing the hash-table parameters through a methodology that incorporates discrete latent and a decoder, as suggested by Girish et al. (2023).

5.4. Learned Regularizations

The visual similarity of the IntraSeismic results to those obtained using the PD-TV method (Figures 3, 5, and 7) stems mainly from the shared use of the TV regularization strategy. Both IntraSeismic and PD-TV exhibit challenges in recovering high impedance layers—a feat where the PnP method showed superiority in the Marmousi example. Such limitations might arise from selecting the regularization term itself, which can inadvertently constrain the framework's modeling capacity, leading to inherent trade-offs like the loss of contrast commonly associated with TV regularization. Therefore, future research should aim to explore learned regularization strategies, including PnP or Regularization by denoising (RED) (Romano et al., 2017), within IntraSeismic-type frameworks.

5.5. Other Applications

The versatility of the IntraSeismic framework (Figure 1) is underscored by its independence from any specific form of (seismic) modeling operator, making it a compelling alternative for a variety of seismic-related inverse problems. While this study has demonstrated its applicability in the context of static and dynamic elastic parameter estimation from post- and pre-stack seismic data, the framework can be easily extended to other reservoir characterization, where for example, one is interested to recover petrophysical parameters (Grana et al., 2021). Traditionally, this involves a sequential approach where elastic and petrophysical parameters are inverted separately or a joint approach where seismic data are inverted directly for petrophysical properties (Bosch et al., 2010; Grana et al., 2021, 2022). More recently, a direct petrophysical inversion method based on optimal basis functions derived from well log data and rock physics models has been proposed in Corrales et al. (2024). Both the sequential and direct inversion methods can be seamlessly integrated within the IntraSeismic framework, using two cascaded IntraSeismic inversion processes that use modeling operators embedding the physics of the seismic and rock physics processes, respectively. Moreover, as demonstrated in the pre-stack seismic inversion case (Section 3.2), utilizing dedicated non-linear mapping modules for each inverted property of interest can lead to improved results. Alternatively, in the case of joint petrophysical inversion, the two modeling operators could be directly concatenated, enabling a direct mapping from petrophysical properties to seismic data.

Expanding the range of seismic applications, IntraSeismic is also applicable to seismic imaging problems such as least squares migration and Full-Waveform Inversion (FWI). In such cases, the modeling component would be able to capture the physics of wave propagation in a linear or non-linear fashion, respectively. Specifically in the case of FWI, the use of INR has already shown promising results as shown by J. Sun et al. (2023).

6. Conclusions

In this study, we have introduced the IntraSeimic framework, a hybrid deep learning-based and model-driven strategy to solve seismic inverse problems. We presented and critically evaluated the IntraSeismic framework by applying it to both realistic synthetic and field pre-stack/post-stack static and dynamic seismic data sets, and benchmarked it against prevalent variational approaches and unsupervised deep-learning-based methods in the seismic inversion domain. Our findings underscore IntraSeismic's superior capability in producing high-resolution impedance models and faster convergence. Additionally, the IntraSeismic framework's inherent coordinate-based parametrization offers revolutionary prospects for the seismic interpretation domain, especially in terms of data access and compression. Finally, the use of MCD within IntraSeismic's MLP component further empowers it to quantify uncertainties, a critical aspect in seismic inversion.

Data Availability Statement

All data sets utilized in this study are publicly available. For the synthetic data, please refer to the SEG Wiki page on Open Data at https://wiki.seg.org/wiki/Open_data. Similarly, for the Sleipner data set, information can be found at https://co2datashare.org/dataset/sleipner-2019-benchmark-model. To reproduce the results, the code is publicly available on GitHub at https://github.com/DeepWave-KAUST/IntraSeismic (Romero et al., 2024).

Acknowledgments
This publication is based on work supported by the King Abdullah University of Science and Technology (KAUST). The authors thank the DeepWave sponsors for supporting this research and Equinor and partners for releasing the 4D Sleipner data set.

References

Aki, K., & Richards, P. G. (2002). *Quantitative seismology*. W. H. Freeman and Company.

Avseth, P., Mukerji, T., & Mavko, G. (2005). *Quantitative seismic interpretation: Applying rock physics tools to reduce interpretation risk*. Cambridge University Press.

Biswas, R., Sen, M. K., Das, V., & Mukerji, T. (2019). Prestack and poststack inversion using a physics-guided convolutional neural network. *Interpretation*, *7*(3), SE161–SE174. https://doi.org/10.1190/INT-2018-0236.1

Bosch, M., Mukerji, T., & Gonzalez, E. F. (2010). Seismic inversion for reservoir properties combining statistical rock physics and geostatistics: A review. *Geophysics*, *75*(5), 75A165–75A176. https://doi.org/10.1190/1.3478209

Brougois, A., Bourget, M., Lailly, P., Poulet, M., Ricarte, P., & Versteeg, R. (1990). *Marmousi, model and data*. European Association of Geoscientists & Engineers (p. cp). https://doi.org/10.3997/2214-4609.201411190

Chadwick, A., Williams, G., Delepine, N., Clochard, V., Labat, K., Sturton, S., et al. (2010). Quantitative analysis of time-lapse seismic monitoring data at the Sleipner CO2 storage operation. *The Leading Edge*, *29*(2), 170–177. https://doi.org/10.1190/1.3304820

Chen, Z., & Zhang, H. (2019). Learning implicit fields for generative shape modeling. *arXiv*. arXiv:1812.02822 [cs]. https://doi.org/10.48550/arXiv.1812.02822

Corrales, M., Hoteit, H., & Ravasi, M. (2024). Seis2rock: A data-driven approach to direct petrophysical inversion of pre-stack seismic data. *Earth and Space Science*, *11*(2), e2023EA003301. https://doi.org/10.1029/2023EA003301

Das, V., Pollack, A., Wollner, U., & Mukerji, T. (2019). Convolutional neural network for seismic impedance inversion. *Geophysics*, *84*(6), R869–R880. https://doi.org/10.1190/geo2018-0838.1

Downton, J. E. (2005). *Seismic parameter estimation from avo inversion* (Doctoral dissertation). University of Calgary. Retrieved from https://www.crewes.org/Documents/GraduateTheses/2005/Downton-PhD-2005.pdf

Doyen, P. (2007). Seismic reservoir characterization: An earth modelling perspective. *EAGE*. https://doi.org/10.3997/9789462820234

Dupont, E., Goliński, A., Alizadeh, M., Teh, Y. W., & Doucet, A. (2021). Coin: Compression with implicit neural representations.

Fehler, M., & Keliher, P. J. (2011). *Seam phase 1: Challenges of subsalt imaging in tertiary basins, with emphasis on deepwater gulf of Mexico*. Society of Exploration Geophysicists.

Gal, Y., & Ghahramani, Z. (2016). Dropout as a Bayesian approximation: Representing model uncertainty in deep learning. In *Proceedings of the 33rd International Conference on Machine learning* (pp. 1050–1059). PMLR. Retrieved from https://proceedings.mlr.press/v48/gal16.html

Gholami, A. (2015). Nonlinear multichannel impedance inversion by total-variation regularization. *Geophysics*, *80*(5), R217–R224. https://doi.org/10.1190/geo2015-0004.1

Girish, S., Shrivastava, A., & Gupta, K. (2023). Shacira: Scalable hash-grid compression for implicit neural representations.

Goli, L., Reading, C., Sellán, S., Jacobson, A., & Tagliasacchi, A. (2023). Bayes' rays: Uncertainty quantification for neural radiance fields.

Goupillaud, P. L. (1961). An approach to inverse filtering of near-surface layer effects from seismic records. *Geophysics*, *26*(6), 754–760. https://doi.org/10.1190/1.1438951

Grana, D., Azevedo, L., de Figueiredo, L., Connolly, P., & Mukerji, T. (2022). Probabilistic inversion of seismic data for reservoir petrophysical characterization: Review and examples. *Geophysics*, *87*(5), M199–M216. https://doi.org/10.1190/geo2021-0776.1

Grana, D., Mukerji, T., & Doyen, P. (2021). *Seismic reservoir modeling cover image seismic reservoir modeling: Theory, examples, and algorithms*. John Wiley & Sons, Ltd. https://doi.org/10.1002/9781119086215

Herron, D. A. (2011). *Seismic interpretation*. Society of Exploration Geophysicists.

Kendall, A., & Gal, Y. (2017). What uncertainties do we need in Bayesian deep learning for computer vision? arXiv. arXiv:1703.04977 [cs]. https://doi.org/10.48550/arXiv.1703.04977

Kingma, D. P., & Ba, J. (2014). Adam: A method for Stochastic optimization. *arXiv*. arXiv:1412.6980 [cs]. https://doi.org/10.48550/arXiv.1412.6980

Lindstrom, P. (2014). Fixed-rate compressed floating-point arrays. *IEEE Transactions on Visualization and Computer Graphics*, *20*(12), 2674–2683. https://doi.org/10.1109/TVCG.2014.2346458

Lipari, V., Picetti, F., Bestagini, P., & Tubaro, S. (2021). Post-stack inversion with uncertainty estimation through Bayesian deep image prior. In *82nd EAGE Annual Conference & exhibition* (Vol. 2021, pp. 1–5). European Association of Geoscientists & Engineers. https://doi.org/10.3997/2214-4609.202112878

Lumley, D. (2010). 4D seismic monitoring of CO2 sequestration. *The Leading Edge*, *29*(2), 150–155. https://doi.org/10.1190/1.3304817

Martin, G. S., Wiley, R., & Marfurt, K. J. (2006). 02). Marmousi2: An elastic upgrade for Marmousi. *The Leading Edge*, *25*(2), 156–166. https://doi.org/10.1190/1.2172306

Mildenhall, B., Srinivasan, P. P., Tancik, M., Barron, J. T., Ramamoorthi, R., & Ng, R. (2020). NeRF: Representing scenes as neural radiance fields for view synthesis. *Computer Vision – ECCV 2020*, 405–421. arXiv. arXiv:2003.08934 [cs]. https://doi.org/10.48550/arXiv.2003.08934

Müller, T., Evans, A., Schied, C., & Keller, A. (2022). Instant neural graphics primitives with a multiresolution hash encoding. *ACM Transactions on Graphics*, *41*(4), 1–15. [cs]. https://doi.org/10.1145/3528223.3530127

Oldebnbur, D., Scheuer, T., & Levy, S. (1983). Recovery of the acoustic impedance from reflection seismograms. *Geophysics*, *48*(10), 1318–1337. https://doi.org/10.1190/1.1441413

Oz, Y., & Miller, R. D. (2015). *Engineering seismology: With applications to geotechnical engineering*. Society of Exploration Geophysicists. https://doi.org/10.1190/1.9781560803300

Park, J. J., Florence, P. R., Straub, J., Newcombe, R. A., & Lovegrove, S. (2019). Deepsdf: Learning continuous signed distance functions for shape representation. *CoRR*. abs/1901.05103. Retrieved from http://arxiv.org/abs/1901.05103

Ravasi, M., & Birnie, C. (2022). A joint inversion-segmentation approach to assisted seismic interpretation. *Geophysical Journal International*, *28*(2), 893–912. https://doi.org/10.1093/gji/ggab388

Ravasi, M., Luiken, N., Romero, J., & Corrales, M. (2023). Deep learning to replace or augment model-based seismic inversion? In *84th EAGE Annual Conference & exhibition* (Vol. 2023, pp. 1–5). European Association of Geoscientists & Engineers. https://doi.org/10.3997/2214-4609.202310158

Ravasi, M., Romero, J., Corrales, M., Luiken, N., & Birnie, C. (2023). Chapter Six - Striking a balance: Seismic inversion with model- and data-driven priors. In S. S. Ganguli & V. P. Dimri (Eds.), *Developments in structural geology and tectonics* (Vol. 6, pp. 153–200). Elsevier. https://doi.org/10.1016/B978-0-323-99593-1.00008-2

Ravasi, M., & Vasconcelos, I. (2020). Pylops—A linear-operator python library for scalable algebra and optimization. *SoftwareX*, *11*, 100361. https://doi.org/10.1016/j.softx.2019.100361

Ricker, N. (1943). Further developments in the wavelet theory of seismogram structure. *Bulletin of the Seismological Society of America*, *33*(3), 197–228. https://doi.org/10.1785/BSSA0330030197

Romano, Y., Elad, M., & Milanfar, P. (2017). The little engine that could: Regularization by denoising (red).

Romero, J., Corrales, M., Luiken, N., & Ravasi, M. (2022). Plug and play post-stack seismic inversion with CNN-based denoisers. In *Second EAGE subsurface intelligence workshop* (Vol. 2022, pp. 1–5). European Association of Geoscientists & Engineers. https://doi.org/10.3997/2214-4609.2022616015

Romero, J., Heidrich, W., Luiken, N., & Ravasi, M. (2024). Seismic reservoir characterization with implicit neural representations. https://doi.org/10.5281/zenodo.11180571

Romero, J., Luiken, N., & Ravasi, M. (2022). *Robust joint inversion and segmentation of 4d seismic data* (pp. 3414–3418). SEG Technical Program Expanded Abstracts.

Romero, J., Luiken, N., & Ravasi, M. (2023). Seeing through the co2 plume: Joint inversion-segmentation of the sleipner 4d seismic data set. *The Leading Edge*, *42*(7), 446–516. https://doi.org/10.1190/tle42070457.1

Rudin, L. I., Osher, S., & Fatemi, E. (1992). Nonlinear total variation based noise removal algorithms. *Physica D: Nonlinear Phenomena*, *60*(1), 259–268. https://doi.org/10.1016/0167-2789(92)90242-F

Russell, B., & Hampson, D. (1991). *Comparison of poststack seismic inversion methods* (pp. 876–878). 61st Annual International Meeting, SEG.

Sansal, A., Kainkaryam, S., Lasscock, B., & Valenciano, A. (2023). MDIO: Open-source format for multidimensional energy data. *The Leading Edge*, *42*(7), 465–473. https://doi.org/10.1190/tle42070465.1

Schiassi, E., Leake, C., De Florio, M., Johnston, H., Furfaro, R., & Mortari, D. (2020). Extreme theory of functional connections: A physics-informed neural network method for solving parametric differential equations. *arXiv*. [physics, stat]. https://doi.org/10.48550/arXiv.2005.10632

Shen, J., Agudo, A., Moreno-Noguer, F., & Ruiz, A. (2022). Conditional-flow nerf: Accurate 3d modelling with reliable uncertainty quantification.

Sheriff, R. E., & Geldart, L. P. (1995). *Exploration seismology* (2nd ed.). Cambridge University Press. https://doi.org/10.1017/CBO9781139168359

Sitzmann, V., Martel, J. N. P., Bergman, A. W., Lindell, D. B., & Wetzstein, G. (2020). Implicit neural representations with periodic activation functions. CoRR, abs/2006.09661. https://arxiv.org/abs/2006.09661

Smith, R., Nivlet, P., Alfayez, H., & AlBinHassan, N. (2022). Robust deep learning-based seismic inversion workflow using temporal convolutional networks. *Interpretation*, *10*(2), SC41–SC55. https://doi.org/10.1190/INT-2021-0142.1

Smith, R. C. (2013). *Uncertainty quantification: Theory, implementation, and applications*. Society for Industrial and Applied Mathematics. https://doi.org/10.1137/1.9781611973228

Steeples, D. W., & Miller, R. D. (1988). *Seismic reflection methods applied to engineering, environmental, and ground-water problems*. European Association of Geoscientists & Engineers. (p. cp). https://doi.org/10.3997/2214-4609-pdb.214.1988_005

Strümpler, Y., Postels, J., Yang, R., van Gool, L., & Tombari, F. (2022). Implicit neural representations for image compression.

Sun, J., Innanen, K., Zhang, T., & Trad, D. (2023). Implicit seismic full waveform inversion with deep neural representation. *Journal of Geophysical Research: Solid Earth*, *128*(3), e2022JB025964. https://doi.org/10.1029/2022JB025964

Sun, Y., Liu, J., Xie, M., Wohlberg, B., & Kamilov, U. S. (2021). CoIL: Coordinate-based internal learning for imaging inverse problems. arXiv. arXiv:2102.05181 [eess]. https://doi.org/10.48550/arXiv.2102.05181

Tancik, M., Srinivasan, P. P., Mildenhall, B., Fridovich-Keil, S., Raghavan, N., Singhal, U., et al. (2020). Fourier features let networks learn high frequency functions in low dimensional domains. arXiv. arXiv:2006.10739 [cs]. https://doi.org/10.48550/arXiv.2006.10739

Tarantola, A. (1984). Inversion of seismic reflection data in the acoustic approximation. *Geophysics*, *49*(8), 1259–1266. https://doi.org/10.1190/1.1441754

Telford, W. M., Geldart, L. P., & Sheriff, R. E. (1990). *Applied geophysics*. Cambridge University Press. https://doi.org/10.1017/CBO9781139167932

Tikhonov, A. N., & Arsenin, V. Y. (1977). *Solution of ill-posed problems*. Winston & Sons.

Ulyanov, D., Vedaldi, A., & Lempitsky, V. (2020). Deep image prior. *International Journal of Computer Vision*, *128*(7), 1867–1888. arXiv:1711.10925 [cs, stat]. https://doi.org/10.1007/s11263-020-01303-4

Vasconcelos, F., He, B., Singh, N., & Teh, Y. W. (2023). Uncertainr: Uncertainty quantification of end-to-end implicit neural representations for computed tomography.

Venkatakrishnan, S. V., Bouman, C. A., & Wohlberg, B. (2013). Plug-and-Play priors for model-based reconstruction. In *2013 IEEE Global Conference on signal and information processing* (pp. 945–948). https://doi.org/10.1109/GlobalSIP.2013.6737048

Wang, D., Gao, J., & Zhou, H. (2019). Data-driven multichannel seismic impedance inversion with anisotropic total variation regularization. *Journal of Inverse and Ill-Posed Problems*, *2018*(2), 229–241. https://doi.org/10.1515/jiip-2017-0024

Wu, B., Xie, Q., & Wu, B. (2022). Seismic impedance inversion based on residual attention network. *IEEE Transactions on Geoscience and Remote Sensing*, *60*, 1–17. https://doi.org/10.1109/TGRS.2022.3193563

Xie, Y., Takikawa, T., Saito, S., Litany, O., Yan, S., Khan, N., et al. (2021). Neural fields in visual computing and beyond. CoRR, abs/2111, 11426. https://arxiv.org/abs/2111.11426

Xu, M., Zhao, L., Gao, S., Zhu, X., & Geng, J. (2022). Joint use of multiseismic information for lithofacies prediction via supervised convolutional neural networks. *Geophysics*, *87*(5), M151–M162. https://doi.org/10.1190/geo2021-0554.1

Yilmaz, O. (2001). *Seismic data analysis*. Society of Exploration Geophysicists.

Zang, G., Idoughi, R., Li, R., Wonka, P., & Heidrich, W. (2021). IntraTomo: Self-supervised learning-based tomography via sinogram synthesis and prediction. In *2021 IEEE/CVF International Conference on Computer Vision (ICCV)* (pp. 1940–1950). https://doi.org/10.1109/ICCV48922.2021.00197

Zhang, K., Li, Y., Zuo, W., Zhang, L., Van Gool, L., & Timofte, R. (2022). Plug-and-Play image restoration with deep denoiser prior. *IEEE Transactions on Pattern Analysis and Machine Intelligence*, *44*(10), 6360–6376. https://doi.org/10.1109/TPAMI.2021.3088914

Zhao, L., Zou, C., Chen, Y., Shen, W., Wang, Y., Chen, H., & Geng, J. (2021). Fluid and lithofacies prediction based on integration of well-log data and seismic inversion: A machine-learning approach. *Geophysics*, *86*(4), M151–M165. https://doi.org/10.1190/geo2020-0521.1

Zheng, J., Ramasinghe, S., & Lucey, S. (2021). Rethinking positional encoding. arXiv. arXiv:2107.02561 [cs]. https://doi.org/10.48550/arXiv.2107.02561

Zoeppritz, K. (1919). Uber reflexion und durchgang seismischer wellen durch unstetigkeitsflächen. Nachrichten von der Königlichen Gesellschaft der Wissenschaften zu Göttingen. *Mathematisch-physikalische Klasse*, 66–84.